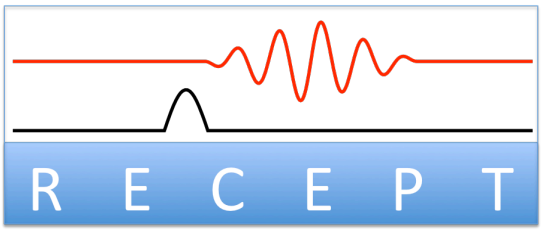

GA No. ACPO-GA-2010-265094
Final REPORT

RECEPT Final report

A. Hanifi (KTH/FOI)

Based on the contributions from:

V.I. Borodulin, A.V. Ivanov, Y.Kachanov, D.A. Mischenko (ITAM)

S.M. Hosseini, R. Örlü, N. Tillmark, P.H. Alfredsson (KTH)

D. de Rosa, R. Donelli (CIRA)

S. Hein (DLR)

J. Pralits (UNIGE)

P. Luchini (UNISA)

H. Kurz, M. Kloker, W. Würz (USTUTT)

G. Schrauf (AIRBUS)

D. Romano (PIAGGIO)

DELIVERABLE No.:

DATE: JUNE 2015

VERSION: FINAL

Objective

This report summarizes the activities performed within the RECEPT project. For details of these activities the reader is referred to the technical reports.

1 Design of experiment

1.1 Wing geometry

The airfoil geometry and the freestream conditions suitable for the planned experiments in the MTL wind tunnel of KTH have been selected to be a wing with the chord length (measured normal to leading edge) of 0.8 m and a free-stream velocity of 10-15 m/s. Investigations were carried out to find an airfoil which provides large enough crossflow *N*-factors at moderate sweep angles and rather low freestream velocities. Moreover, this airfoil should also be suitable for experimental studies at different angles of attack where Tollmien-Schlichting instability is dominant, As a starting point various airfoils available in literature (e.g. HQ 26, ONERA D, NLF(2)-0415, NACA 66_4-221, NACA 67_1-215, NACA 3 and 4 digit families) were considered and their instability characteristics at different freestream conditions were analysed. Studies were performed by DLR and FOI, focusing on different airfoil.

DLR computed the pressure distributions for the corresponding unswept conditions using the MSES code of M. Drela with prescribed maximum transition locations on the lower and upper side. For the boundary-layer computations at infinite swept-wing conditions the COCO code was used. An interface between the two codes had to be developed which also transformed the data from unswept conditions to the chosen sweep angle. For the linear stability analyses the LILO and NOLOT codes were used, supplemented by a preliminary analysis of the instability characteristics based on the ONERA database method. For selected cases the pressure distributions extracted from MSES and transformed to infinite-swept wing conditions were cross-checked by RANS computations using the TAU code. In a second step, the most suitable airfoils taken from previous analysis were modified in order to further adapt their characteristics. The finally chosen airfoil geometry consists of an upper side taken from NACA 67_1-215 and a lower side designed by the University of Stuttgart and FOI. Furthermore, for selected conditions the influence of the lower and upper wind tunnel walls was taken into account. Their influence on the swept-wing pressure distribution was simulated using MSES and again cross-checked by RANS computations (Figure 1). The very low Mach number in combination with the presence of wind tunnel walls lead to very slow convergence rates in the RANS computations when using the compressible TAU code. Therefore, the incompressible DLR RANS code THETA developed for internal flow was used in addition.

In the preliminary analysis by FOI, the NACA airfoils were modified to optimize the location of neutral stability point as well as to maximize the growth of cross-flow modes. Later, we concentrated on the NLF(2)-0415 airfoil. A parametric study was performed varying the angle of attack and free-stream velocity for a 35 degrees sweep angle and a chord of 0.8 m. Further, some computations were performed for 45 degrees sweep angle, too. The work included calculation of inviscid flow (panel method), boundary-layer profiles and stability analysis using the NOLOT code.

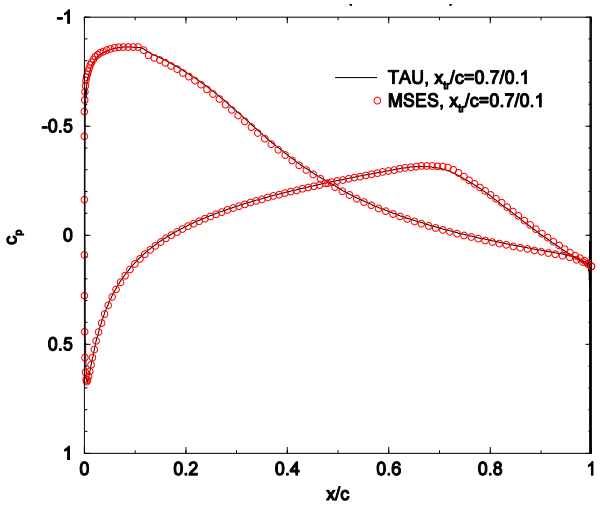

Figure 1: Pressure distribution of the modified NACA 671-215 airfoil at about -4.1o angle of attack, 35o sweep angle and free-stream velocity of 15 m/s with prescribed laminar-turbulent transition at 70% chord on upper side and 10% chord on lower side. Comparison of TAU and MSES results.

In the final period of the work, based on the DLR's work, the NACA 67_1-215 airfoil was chosen as the best candidate. The lower side of the airfoil was then modified by USTUTT to delay the laminar separation. FOI performed the analysis for the modified geometry placed inside the KTH wind tunnel to include the effects of the tunnel walls. The computations include RANS (using Edge code), boundary-layer and PSE computations.

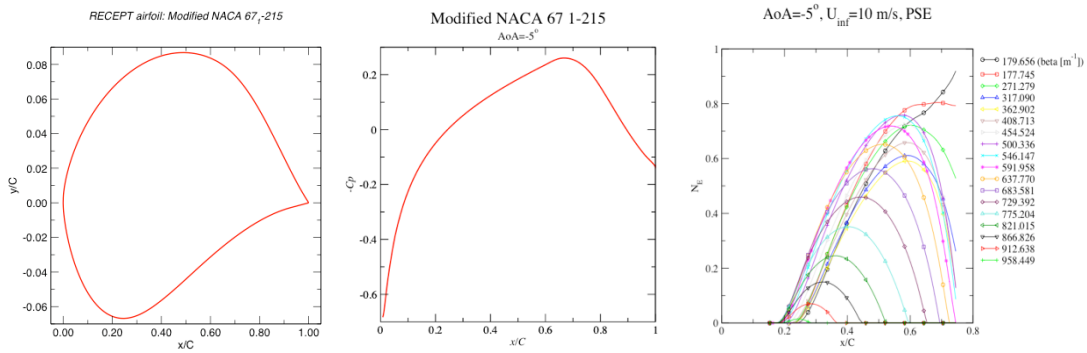

Figure 2: Geometry, pressure distribution and the nonlocal N-factors for RECEPT airfoil at -5o angle of attack and 35o sweep angle. Free-stream velocity is 10m/s.

The modified NACA 67_1-215 (Figure 2) was then selected by DLR and FOI as the final geometry and delivered to USTUTT (on June 17, 2011) with a proposed location of pressure distributions.

1.2 Design of wind tunnel sidewalls

In order to guarantee good spanwise inhomogeneity of the flow over the wing, countoured sidewalls need to be designed. This was done by PIAGGIO in collaboration with FOI. The following approach was used by PIAGGIO:

- Generation of a parametric CAD model for the swept-mounted wing installed in the wind tunnel with flat walls.
- CFD mesh generation associated to the CAD model.
- CFD flow simulations for the "infinite span" WT model, replacing solid sidewalls with periodic boundaries.

- Extraction of typical streamlines shape from the CFD solution back to the CAD environment.
- CAD design of the contoured sidewalls based on the reference streamline.
- CFD mesh generation for the contoured WT configuration.
- Flow simulation for the contoured WT configuration.

A fully parametric CAD model developed in CATIA v5 R19 is used to design the sidewalls. The starting swept-mounted airfoil is obtained through a best fitting of about 600 points defining the airfoil shape. In particular, a 5th order NURBS with 19 control points has been used. Figure 3 shows a view of the parametric CAD model. The model is mounted vertically, and positioned at mid-length of the test section. The rotation axis for angle of attack modification is parallel to the leading edge.

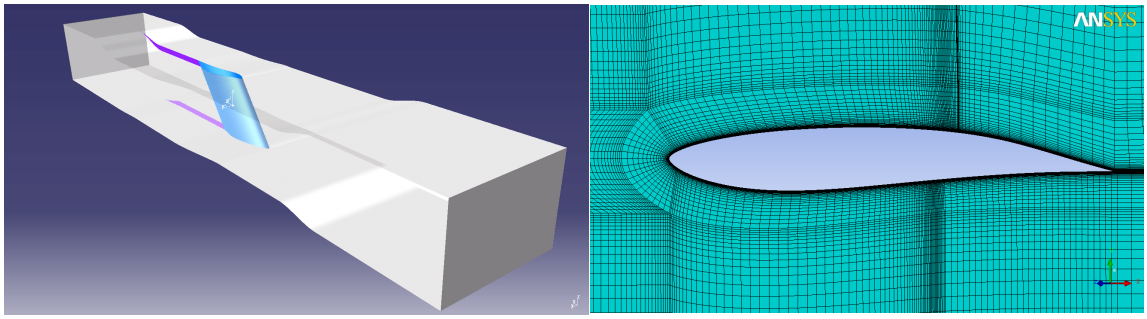

Figure 3: Overview of the CAD model (left) and CFD mesh (right).

CFD evaluations have been performed using CFD++, the commercial CFD code used by Piaggio Aero Industries, which is based on the finite volume method. A 2nd order spatial discretization has been used with a multigrid technique (4 W-cycles on 20 levels) to accelerate the convergence. The boundary layer has been integrated directly to the wall around all solid boundaries. The 3-equations Goldberg's κ-ε-Rt turbulence model has been applied. In the grids used here, the y+ was of order of unity around all solid adiabatic viscous walls. Sea level ISA conditions have been considered to define the values of the ambient temperature and pressure. A WT inlet mass flow rate equal to 11.76 kg/s has been imposed. Transition has been imposed at 70% of chord length on the upper side and at 10% on the lower side.

The sidewalls were designed for the two different angles of attack corresponding to conditions of Experiments A and B (-5.0° and +1.5°). The design of sidewalls for +1.5° angle of attack showed to be more demanding. The first design did not fulfil the targets. Several contour have been designed in order to find the best bi-dimensional design able to satisfy the infinite swept-wing approximation. The final designed showed good parallelism of isobars except for areas close to the intersection of the model to the wind tunnel walls. However, this is not a big issue, since to perform the present WT tests it is enough that the isobars are parallel to the leading edge in the central area of the model itself. This condition is respected by both the designs carried out at AoA of -5° and +1.5°. In particular, for the negative angle of attack case the isobars look perfectly parallel on the upper side, but not on the lower (see Figure 4). For the positive angle of attack case the isobars on the upper surface are not looking perfectly parallel close to the leading edge. This is mainly due to small variation of pressure in an area with a small pressure gradient.

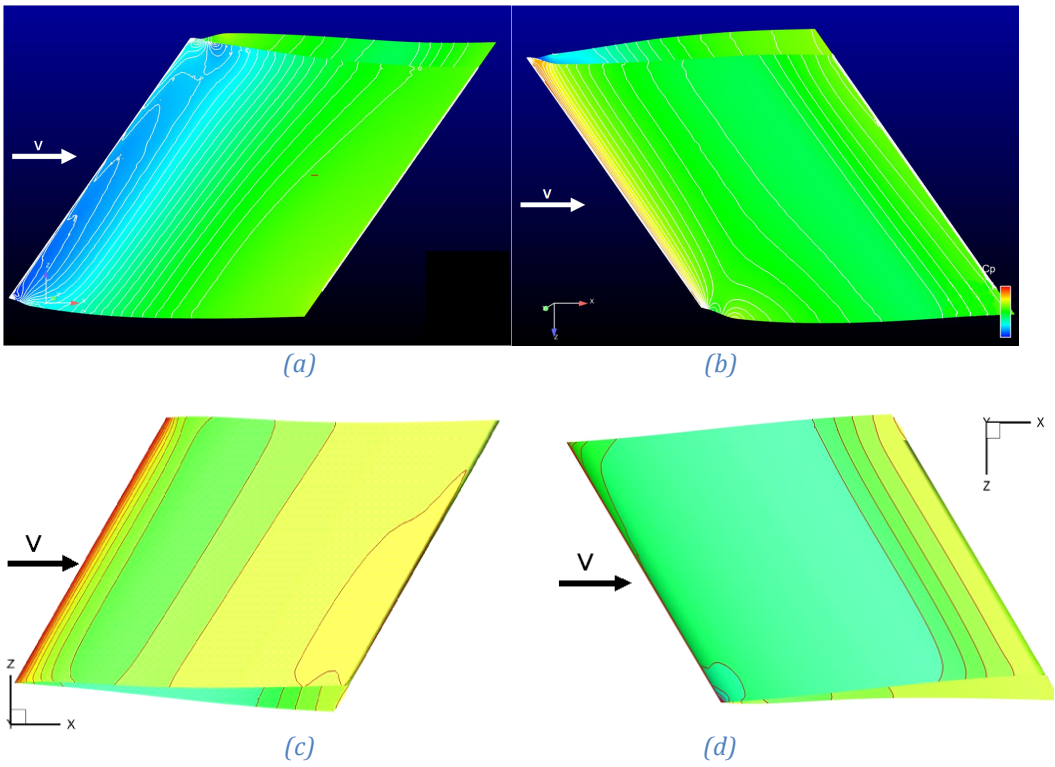

Figure 4: Isobars on the (a) lower surface for a rotation of -5°, (b) upper surface for a rotation of -5°, (c) lower surface for a rotation of +1.5°, (d) upper surface for a rotation of +1.5°.

Due to the requirements related to installation of the measurement and perturbation generators, the design of the sidewalls for Experiment A, previously performed by PIAGGIO, should be redone. A CAD file with the new geometry was generated. Further, to check the flow field with the new sidewalls (with higher flow blockage) simulations were performed. The grid was generated for the wing installed in the wind tunnel with new design of sidewalls. RANS computations with prescribed transition point (close to predicted separation on the wing) were performed. Pressure distributions at different spanwise cross sections are shown in Figure 5. The effects of changes in height of open area of wind tunnel were more than expected.

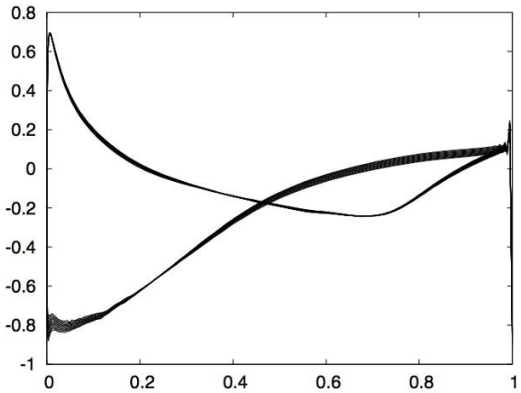

Figure 5: Cp distribution along 11 sections (z=-0.1 to z=0.1 m).

2 Manufacturing of wing models

Two identical swept-wing wind-tunnel models were manufactured by group of Stuttgart University (USTUTT). For the manufacturing process the wind tunnel model was built as a 2D airfoil section and then cut on both sides under an angle of 35° to provide the necessary sweep angle. The model was manufactured in NC-milled negative molds. The material for those molds is SIKA SLABS M610, a polyurethane foam with a very high density. A special milling technique with an inclined face cutter provides a surface roughness smaller than +0.02mm. This roughness is smoothed by carefully sanding until all milling tracks disappear. Then epoxy resin is used to remove the porosity of the surface. The mold is prepared with release agent and then UP-coating resin (Larit T-35) is sprayed into the mold.

The skin of the models is built as a symmetrical carbon-fiber/glass-fiber/carbon-fiber sandwich with 5mm wall thickness. To reach the desired smoothness, it is finished with wet sanding (grit No.1200) and polished (Rot-Weiß-Paste). The surface roughness was measured with a high precision surface measurement device (DIAVITE DH-5). The outcome of the roughness measurement can be quite sensitive to the settings of the device, mainly if a mixture of roughness and waviness is present. The discrimination between roughness and waviness is done by a predefined high pass filter implemented in the measurement device. This filter was set to the longest possible distance, which corresponds to 2.5mm (roughness elements with dimensions larger than this value are treated as waviness). Two scans were conducted with measurement length set to 15mm, which is the maximum. Mean roughness values of 0.98μm were obtained.

The airfoil is equipped with arrays of static pressure taps for measurements and adjustment of the chordwise pressure distributions. Parts of its surfaces are covered with graphite to make them electroconductive (Figure 6).

Figure 6: Airfoil with slot and carbon cover.

3 Design of disturbance sources and measurement system

In order to perform the present controlled experiments and to acquire the experimental data, it was necessary to design, manufacture, and apply the following additional equipment (besides the experimental model briefly described above): (*i*) a source of controlled nonuniformities of the airfoil surface providing excitation of vibrations in broad ranges of frequencies and spanwise wavenumbers, (*ii*) a source of fully controlled, time-periodic, spanwise-uniform freestream vortices working in the desired frequency range, and (*iii*) a traversing mechanism adopted for precise positioning of the hot-wire probe in the vicinity of notably 3D surface of the swept-wing airfoil, which would produce as weak flow blockage as possible and would be especially suitable for traversing the hot-wire probe along the span of 35-degree swept wing model at exactly constant (within every scan) wall distances. The designed and manufactured equipment required also some special hardware and software for the traverse control, generation and amplification of input signals to the disturbance generators, data acquisition, and preliminary data analysis and display. In particular, a multi-channel system of computer-aided generation and amplification of the disturbance sources' signals was required. A description of the equipment designed and used in the present experiment is given below.

3.1 Traversing system

The main (standard) traversing mechanism of the MTL wind-tunnel was mainly adopted for measurements on classical horizontally mounted flat plates. Moreover, it can perturb the base flow and change the freestream speed during its movements by variation of total blockage of the wind-tunnel test section. In order to solve both the problem of the MTL-traverse influence and the task of precise hot-wire traversing on a vertically mounted swept airfoil it was suggested to use the standard MTL traverse only partly and to keep it during main measurements as far downstream the airfoil as possible. In addition a decision was made to equip the main traverse with another, additional, smaller traverse (called 'Komarik'), which would be mounted on a very long sting and abut on the airfoil surface.

The additional traverse had to satisfy the following requirements: (*i*) to have very small cross-section, in order to eliminate any significant baseflow distortions, (*ii*) to have firm bearing onto the airfoil surface for minimization of probe vibrations, (*iii*) to have statically determinate bearing on curved airfoil surface at any position on measurements (to have three legs), (*iv*) to be well adopted for convenient measurements of great number of spanwise profiles along oblique axis (inclined at 35 degree), (*v*) to have spanwise range of probe positioning of at least 130 mm (without displacement of the large standard MTL traverse) with accuracy of about ±20 microns or better, (*vi*) to provide good constancy of wall-normal distance (of several microns) while performing spanwise scans, and (*vii*) to have wall-normal range of probe positioning of about 50 mm with accuracy of about ±5 μm or better.

The development of such traverse was a very difficult task, which had been solved successfully. The traverse fully satisfying these rather conflicting requirements was designed and manufactured in Novosibirsk group and was called 'Komarik' (which means in Russian a kind of a small mosquito with a long proboscis). 'Komarik' design includes an oblique spanwise bar, adjusted for spanwise measurements on 35 degree swept wings (Figure 7 top-left), two rear legs for bearing onto the airfoil surface, a very compact and precise *y*-mechanism (Figure 8 left) for displacement of the hot-wire probe in the wall-normal direction with accuracy of the probe positioning about 3 microns. A small leg at *y*-mechanism provides the third surface bearing which makes the traverse standing stable. Both *y*- and *z*'-mechanisms of 'Komarik' are equipped with miniature stepping motors with gearboxes (15 mm in diameter). The traverse has a very compact design and especially extremely small cross-section (Figure 7 top-right), which minimizes probable flow blockage and distortion.

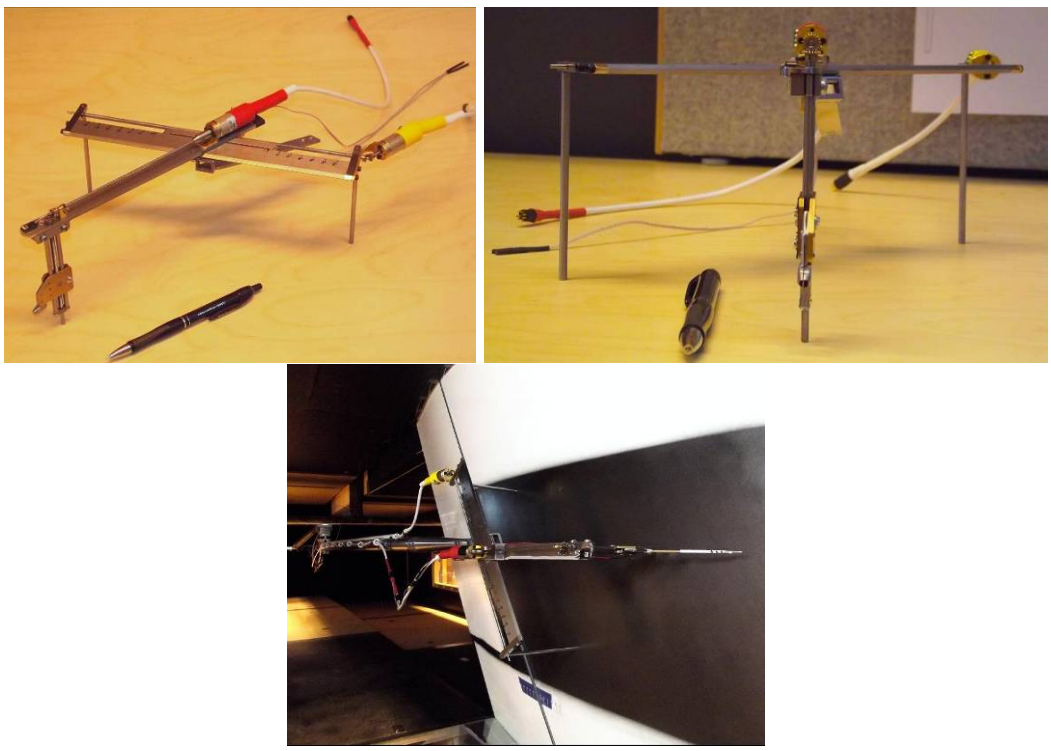

Figure 7: . 'Komarik' traverse in two projections on a desk (top plots) and on the airfoil surface (bottom) equipped with hot-wire probe. Note the very significant downstream offset of main traverse.

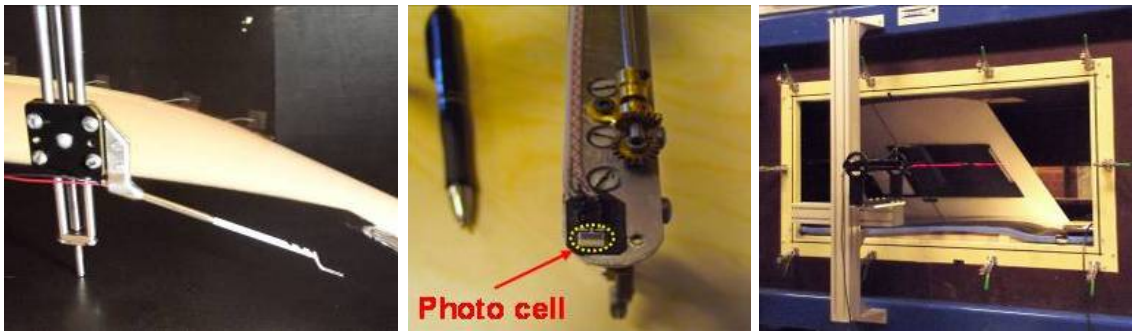

Figure 8: Parts of y*-mechanism of 'Komarik' traverse equipped with hot-wire probe (*left*) and photo sensor (*middle*) and a laser sheet for providing reference spanwise position at traversing (*right*).*

'Komarik' was integrated with the main MTL traverse. Main function of the standard MTL traverse was to deliver 'Komarik' traverse to the position where serial y- or z'-scans were performed, and to "land" it accurately to the airfoil surface. A specially designed electro-mechanical system mounted on the main MTL traverse held a long carbon-fiber sting that held 'Komarik' at its other end. The same system provided a constant prescribed pressing of 'Komarik' onto the airfoil surface and kept the sting parallel to the test-section walls. Final complex traversing system 'Komarik + MTL-traverse' had in total 5 controllable degrees of freedom and required specialized software which was developed by KTH group.

It is necessary to note, that since we were forced to use very long sting (with limited stiffness) in the described traversing system, the spanwise positioning of 'Komarik' landed onto the airfoil surface was determined not very accurately and, therefore, we had to find a reference point while performing spanwise scans. This was achieved by equipment of 'Komarik' with a photo sensor (Figure 8 middle) used in combination with a stationary horizontal laser sheet mounted on the wind-tunnel test section (Figure 8 right). In every spanwise profile the photo sensor of 'Komarik' crossed the stationary laser sheet enabling detection of exact spanwise position of the hot-wire probe. In this way we were able to match all spanwise scans precisely with each other.

Actual position of the hot-wire probe and its orientation in space are determined by settings of the main traverse and the 'Komarik' traverse standing on a curved surface of the swept airfoil section. The conversion of those settings into Cartesian coordinates requires rather bulky calculations. Therefore such calculations were arranged and carried out by means of specially developed MatLab codes 'Komarik_A' and 'Komarik_B' for experiments 'A' and 'B', respectively. The difference between these functions lies in content of their complementary mat-files, which hold all required constants describing the model geometry, the 'Komarik' geometry and the hot-wire probe installation with respect to 'Komarik' (in total, it was about 1000 values in 30 variables). These functions accept also readout of the photo sensor and perform calculation of the true spanwise position of the hot-wire probe based on detection of the laser sheet location. Besides Cartesian coordinates, both functions return 'chord position', coordinate counted along the model surface, and the vector describing the hot-wire orientation with respect to the coordinate system.

3.2 Perturbation generators

As was indicated above, the experiments 'A' and 'B' were performed at fully controlled disturbance conditions. Two kinds of external perturbations were used for excitation of CF-instability modes (in experiments 'A') and 3D TS-waves (in experiments 'B'): (*a*) the surface disturbance source and (*b*) the source of fully controlled freestream vortices.

The main mechanical part (the body) of the surface disturbance source (Figure 9 left) was designed and manufactured in ITAM (Novosibirsk) and later was integrated into the airfoil model (Figure 9 right) and used in both stability and receptivity experiments. The surface perturbations were produced

by means of a spanwise row of circular latex membranes mounted flush with the surface and oscillating (Figure 9 right) under the influence of pressure fluctuations excited by a set of loudspeakers playing role of pumps (Figure 10 left). The speakers were located outside the wind-tunnel test section and were connected to the source by an array of plastic pipes (Figure 10 left). The spanwise step of the membranes λ'_z was selected be equal to 8 mm in the main measurements. In different regimes of measurements either all membranes of part of them (including important case of one membrane) were activated. Depending of the level of excitation, the membranes oscillated with amplitudes from tenth of a micron to more than one hundred microns. The surface disturbance source was mounted flush with the wall at a chord position of 120 mm.

*Figure 9: Source of surface nonuniformities: main body with latex membrane (*left*) and instantaneous picture of membranes deflected during oscillations in the wind tunnel (*right*).*

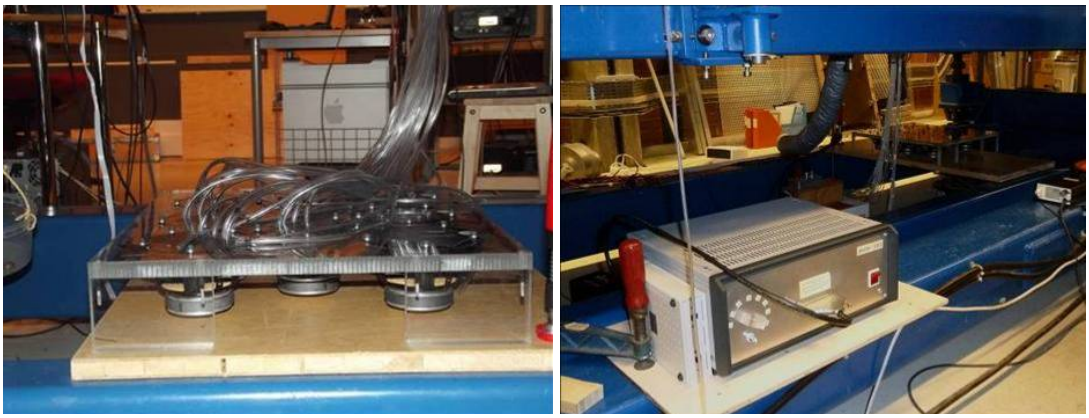

*Figure 10: System of excitation of disturbance sources. Block of speakers with plastic pipes (*left*) and multi-channel disturbance generator with power amplifier (*right*).*

The main part of the freestream vortex generator was also designed and manufactured by Novosibirsk group (Figure 11). The vortices were generated by a thin gilded tungsten wire oscillating in the free stream at desired amplitude and frequency. The wire had a very small diameter (of 50 microns) that ensured absence of uncontrolled von Karman Vortex Street behind it. The controlled freestream vortices were produced by the wire wake oscillating together with the wire in the direction perpendicular to the free stream and to the airfoil leading edge. The amplitude of the velocity fluctuations within the produced vortex street was of order of several tenth of a percent of the mean flow velocity. The wire oscillations were driven by two specially designed electromagnetic shakers (Figure 11) fed from the same generator and amplifier as those used for the excitation of surface nonuniformities (Figure 11 right). These shakers, together with the system of adjustment of the wire positioning and tension, provided extremely stable characteristics of the generated freestream vortices, including their frequencies, amplitude and phase, spanwise uniformity, and the vortex street offset with respect to the airfoil leading edge.

*Figure 11: Source of freestream vortices: upper shaker and vibrating wire in front of the airfoil leading edge (*left*), lower shaker (*right*).*

3.3 Data acquisition

There were 10 most important types of measurements and kinds of data acquisition performed in the experiments 'A' and 'B': (*i*) measurement of the incident flow velocity by Pitot-Prandtl tube, (*ii*) tuft visualization of separated zones, (*iii*) rough transition location detection by a "stethoscope" device, (*iv*) pressure-tap measurements of chordwise distributions of static pressure along the airfoil surface, (*v*) main measurements with single-hot-wire probe mounted on 'Komarik' traverse, (*vi*) two-component velocity measurements in the potential-flows near the boundary-layer edge with the help of a wake-wire technique, (*vii*) two-component potential-flow measurements at a distance from the airfoil by means of X-hot-wire probe, (*viii*) complementary two-component potential-flow measurements at a distance from the airfoil by means of PIV approach, (*ix*) point measurements of amplitudes of oscillations of the surface disturbance source membranes performed in their centres inside the wind tunnel, and (*x*) measurements of shapes of bending of membranes during oscillations performed in ITAM after completion wind-tunnel experiments.

4 Experiments

4.1 Adjustment and tests of experimental setup and base flow measurements

As part of the experimental activity of the KTH group a test-section mock-up was designed and build in order to test all hardware related issues prior to the real, time-limited, experiments in the MTL wind tunnel. For experiments A & C, the sidewalls were designed and fabricated out of plywood to provide a robust and reusable solution on which one can stand to manipulate equipment in the vicinity of the model (see Figure 12). For Experiment C, which required different sidewalls, some plywood parts were replaced by expanded polystyrene that made the production procedure much faster.

Figure 12: Test section mockup, ceiling and floor pieces (jig saw puzzle), model and sidewalls in MTL wind tunnel.

An accurate installation of the rated geometrical angle of attack of the swept airfoil under study was performed in the MTL wind-tunnel test section (ITAM, KTH) by means of a special system of the airfoil mounting designed, manufactured, and mounted by KTH and by means of a special installation technique developed by ITAM.

During the first measurement campaign (February/March 2012) planar (2D) particle-image velocimetry (PIV) measurements were performed to obtain a global idea of the baseflow on the working side of the model. For this purpose a three axis automatic traversing system was installed and around 30 velocity fields in two parallel planes to the model with a field of view of 160mm x 160mm were acquired covering the area of the airfoil on which hot-wire measurements will be performed in the future (cf. the graphite-coated area in Figure 13).

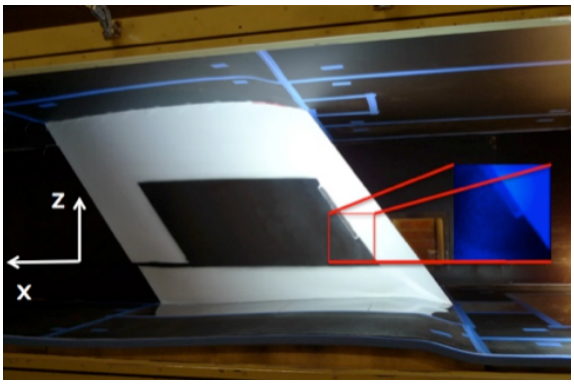

Figure 13: Field of view for one PIV measurement location.

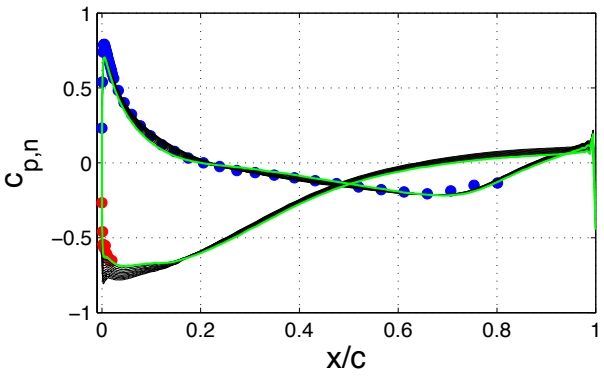

Figure 14: Measured and computed Pressure distribution.

During the same measurement campaign, a number of pressure measurements were conduction for which a new high accuracy pressure transducer in conjunction with a mechanical ScaniValve were used. Besides the hardware part, the software implementation was provided in LabView. Various pressure scans were performed to check repeatability and statistical convergence, and assess the uncertainty. Additionally, the effects of upstream disturbances, possible leakage, tripping close to the trailing edge and the sensitivity to inaccuracies in the aligned angle of attack (AOA) were investigated. The result of around 20 scans at the same AOA ensured confidence in the obtained results as apparent from the pressure distributions shown in Figure 14, where also a comparison with the simulation results are given.

All components of the experimental model (with the airfoil equipped with disturbance sources) have been assembled and installed inside the test-section of the MTL wind tunnel at KTH Mechanics in two series of experiments. In the first series, the airfoil was installed at −5-degree angle of attack to provide conditions of predominant amplification of crossflow instability modes planed for investigation in experiments ‘A’ and ‘C’. In the second series, the angle of attack was equal to +1.5 degree with predominant amplification of Tollmien-Schlichting instability modes planed for investigation in experiments ‘B’.

Four main types of the base-flow measurements have been performed: (i) pressure-tap measurements, (ii) x-hot-wire two-component potential-flow velocity measurements at relatively large distances from the airfoil surface, (iii) hot-wire and wake-wire two-component velocity measurements just above the boundary-layer edge, and (iv) one-component hot-wire measurements inside the boundary layer. The most detailed measurements at conditions of experiments ‘A’ were carried out at the incident flow velocity of 10 m/s, while at conditions of experiments ‘C’, some of measurements were performed also at higher free-stream speeds. It was found that in absence of turbulence-generating grids the potential-flow structure is speed independent.

Detailed comparison of the simulated and computed flow fields were performed. The pressure coefficient from RANS simulations were compared to those measured in experiments (see Figure 15), showing a good agreement.

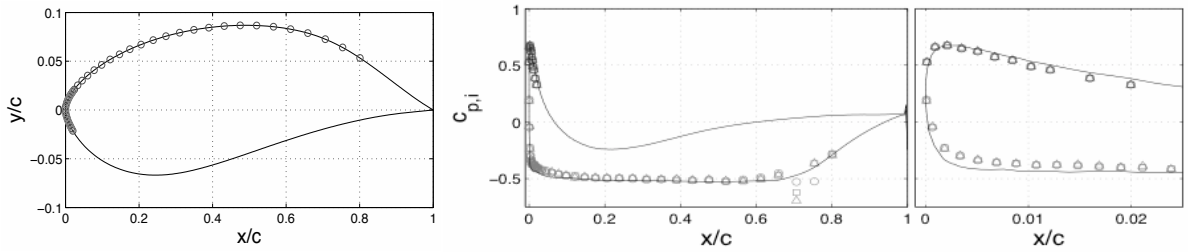

Figure 15: Location of pressure taps (left) and comparison of measured and computed pressure distributions at the 1.5º angle of attack case. Curves are from the RANS calculations and the symbols from the experiments.

Further investigations were made by extracting the flow field from the RANS simulations at the exact locations of experimentally measured planes. The flow filed was scaled to match the correct inflow condition and compared to those of measured one (see Figure 16).

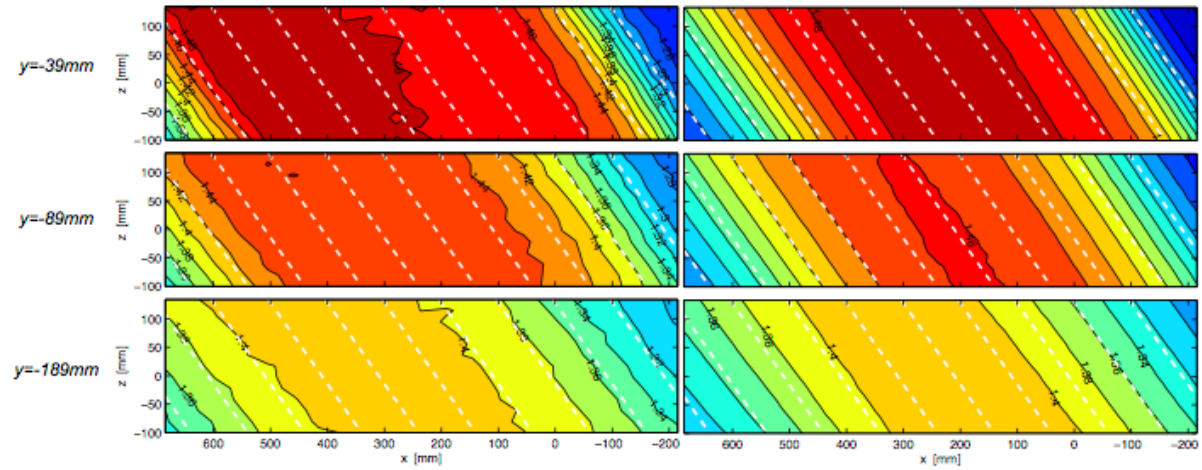

Figure 16: Comparison of measured (left) and computed (right) streamwise velocity distributions at three different x-z planes above the wing for the 1.5º angle of attack case. The data is normalized with the incoming flow velocity.

Measurements (iii) were performed by means of a combination of one-component hot-wire measurements and additional measurements of the potential-flow streamlines with the help of a wake-wire technique developed previously in ITAM. Three wake-wires were mounted in the flow in every experiment (either 'A' and 'C' at airfoil AoA = -5 degree or 'B' at airfoil AoA = +1.5 degree). Shown in Figure 17 (left) is an example of a set of spanwise distributions of streamwise component of the mean velocity vector measured just outside the boundary-layer edge at various chordwise locations. The shapes of the measured potential-flow streamlines are presented in Figure 17 (right) along with the corresponding average shape. It is seen that the streamlines are practically the same at all studied spanwise coordinates. This results supports the conclusion on the spanwise uniformity of the base flow and satisfaction of the sweep condition in the region of main stability and receptivity measurements (in experiments 'A').

In Figure 18 (left) measured and external velocities are compared with the computations performed by FOI. A rather good agreement between the experimental and theoretical results is observed. It is seen also that the sweep condition W′ = const. is satisfied very well in both experiment and computations.

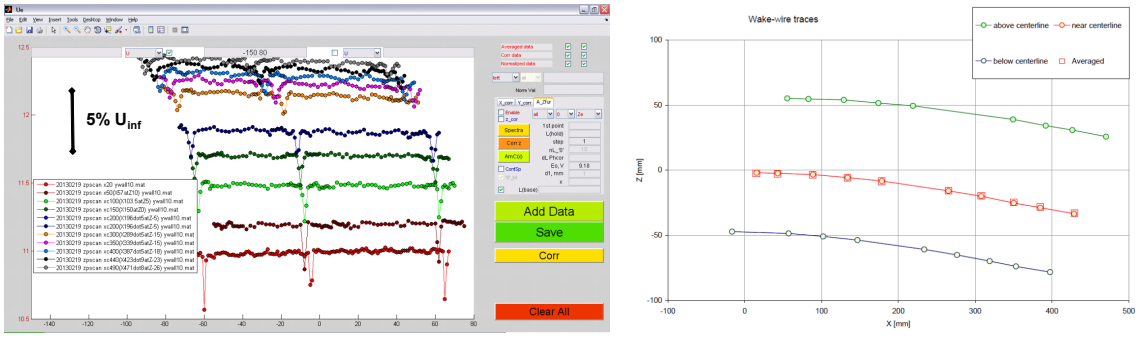

Figure 17: Left: Spanwise uniformity of the potential flow and laminar wakes produced by wake-wires measured in experiment 'A' at xc-xco = 20 to 490 mm. Right: Streamlines of potential flow over airfoil surface measured by wake-wires in experiments 'A' (AoA = -5 degree).

The results of measurements and calculations (FOI) of shapes of the wall-parallel velocity profiles of the streamwise component of the mean-velocity vector are illustrated in Figure 18 (right) for three spanwise positions. It is seen, first, that the experimental and theoretical profiles agree very well with each other and, second, do not display any spanwise dependence of their shape, in supporting again the result on the observed spanwise uniformity of the base flow inside the boundary layer in the region of main stability and receptivity measurements under conditions of experiments 'A'. Similar results were found for other experiments.

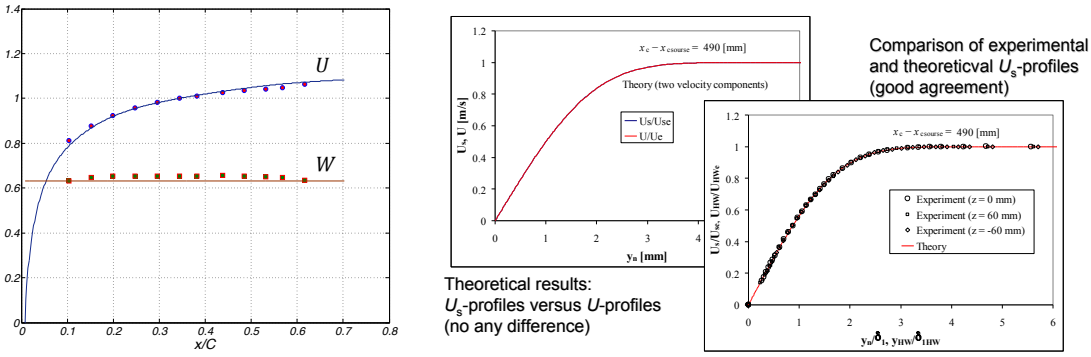

Figure 18: Left: Measured and calculated streamwise distributions of chordwise and spanwise components of potential-flow velocity just outside boundary-layer edge. Right: Measured wall-parallel mean-velocity profiles in comparison with calculated ones. Experiment 'A', x_c-x_{co} = 490 mm.

4.2 Experiments A: excitation of CF-waves

The experiments devoted to study of excitation and development of unsteady (in general) CF-instability modes in the swept-airfoil boundary layer have been performed successfully at AoA of −5 degree, i.e. at the conditions of experiments 'A' (and partly 'C'). They consisted of two main stages: (i) the CF-instability measurements and (ii) the boundary-layer receptivity measurements for the case of excitation of CF-modes.

During the instability measurements 'A' the unsteady (in general) CF-modes were generated by the surface disturbance source developed in the framework of the project RECEPT. The excited time-periodic perturbations were either spanwise periodic, when all membranes of the source were activated, or spanwise localized ones, when only one membrane oscillated. In the latter case the spanwise wavenumber spectrum of the excited CF-modes was broadband while in the former case only two modes (with spanwise wavenumbers $\pm\beta_1$) were excited.

Ranges of the studied disturbance frequencies and spanwise wavenumbers were selected based on preliminary linear-stability calculations performed by DLR at a stage of the experimental model design. The surface disturbance source had spanwise period of membranes of λ'_z = 8 mm

corresponding to maximum spanwise wavenumbers of the spanwise-periodically excited CF-instability modes $\beta_{max} = \pm 2\pi/\lambda'_z = \pm 0.785$ rad/mm. Of course, in case of localized excitation, with only one membrane actuated, the spanwise-wavenumber range of the excited CF-modes was much broader.

The receptivity problem 'A' (excitation of CF-waves) has been studied with the following parameters varied: (*i*) free-stream vortex frequency, (*ii*) surface roughness frequency, (*iii*) difference-mode frequency, (*iv*) sum-mode frequency, (*v*) spanwise wavenumber (spatial scale) of surface nonuniformities and excited CF-waves (i.e. the propagation angle of the latter). The complete lists of regimes studied in the receptivity experiments 'A' are presented in Table 1 and Table 2. Note that the cases with quasi-stationary frequency of surface nonuniformity $f_{sur} = 2.0$ Hz corresponds physically to scattering of freestream vortices on surface roughness.

Names of Regimes	f_{sur} [Hz]	f_{vor} [Hz]	f_{CF-} [Hz]	f_{CF+} [Hz]
Regime 1	65	40	25	105
Regime 2	85	40	45	125
Regime 3	105	40	65	145
Regime 4	67	65	2	132
Regime 5	80	65	15	145
Regime 6	110	65	45	175
Regime 7	140	65	75	205

Table 1: Studied receptivity 'A' regimes with spanwise-localized *surface non-uniformities.*

Names of Regimes	f_{sur} [Hz]	f_{vor} [Hz]	f_{CF-} [Hz]	f_{CF+} [Hz]	λ_z' [mm]
Regime M1-16	67	65	2	132	16
Regime M1-8	67	65	2	132	8
Regime M2-16	20	65	45	85	16
Regime M3-16	8	65	57	73	16
Regime M4-16	2	65	63	67	16
Regime M3RS-16	8 (Reduced Surf. amplitude)	65	57	73	16
Regime M4-8	2	65	63	67	8

Table 2: Studied receptivity 'A' regimes with spanwise-periodic *surface non-uniformities.*

The instability data were subjected to a deep mathematical processing. The obtained instability characteristics were determined in Fourier space for every particular harmonic of the frequency-spanwise-wavenumber spectrum and, hence, they are independent of the specific way of excitation (as usually in the linear instability problem).

The measurements have shown that in the studied range of parameters the shape of the membranes' oscillation is: (*i*) independent of frequency, (*ii*) independent of amplitude, and (*iii*) independent of the particular membrane. In addition, it was found that the phase of the oscillations is always constant with high accuracy along the membrane surface. This means that the shape of membrane bending during oscillation period (Figure 19 left) remains the same at every time instant. The results of detailed shape measurements turned out to be approximated very well by an analytical solution found previously in ref. [75] (section 98, page 451, large bending) for static bending of thin membranes as seen in Figure 19 (right). The corresponding formula is indicated in the plot.

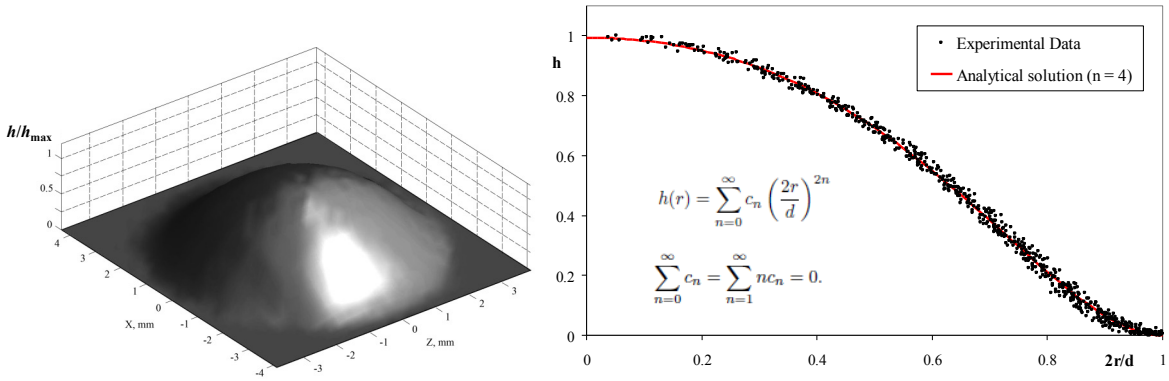

*Figure 19: Magnified instantaneous shape of bending of membrane # 13 during oscillations (*left) and *measured normalized amplitude distribution of membrane oscillations versus radial distance and its approximation by theoretical solution obtained for problem of small static bending of thin membranes.*

Shown in Figure 20 two examples of CF-mode eigenfunctions measured for arepresented. Based on such measurements the values of wall-normal distances of the CF-modes' amplitude maxima were estimated for every disturbance frequency. These distances were used than during the main instability measurements 'A' performed in regimes with the spanwise-localized excitation of CF-modes by a single membrane of the surface disturbance source.

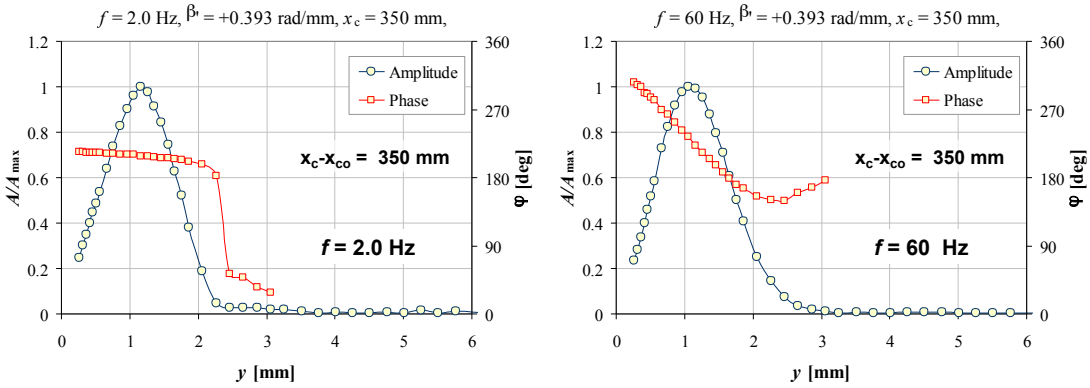

Figure 20: Measured eigenfunctions (amplitudes and phases) of the CF-instability modes excited at lowest and highest frequency studied in stability experiments 'A'.

The linearity of the results were checked by performing a set of experiments with all parameters being the same except the amplitude of membrane excitation which was changed by a factor of two. Two pairs of spanwise distributions of disturbance amplitudes and phases were measured inside the boundary layer (at U/U_e = 0.68) at two chordwise coordinates: x'_s = 170.9 and 399.6 mm (i.e. at distances $x_c - x_{co}$ = 50 and 350 mm downstream the surface disturbance source). These distributions are presented in Figure 21.

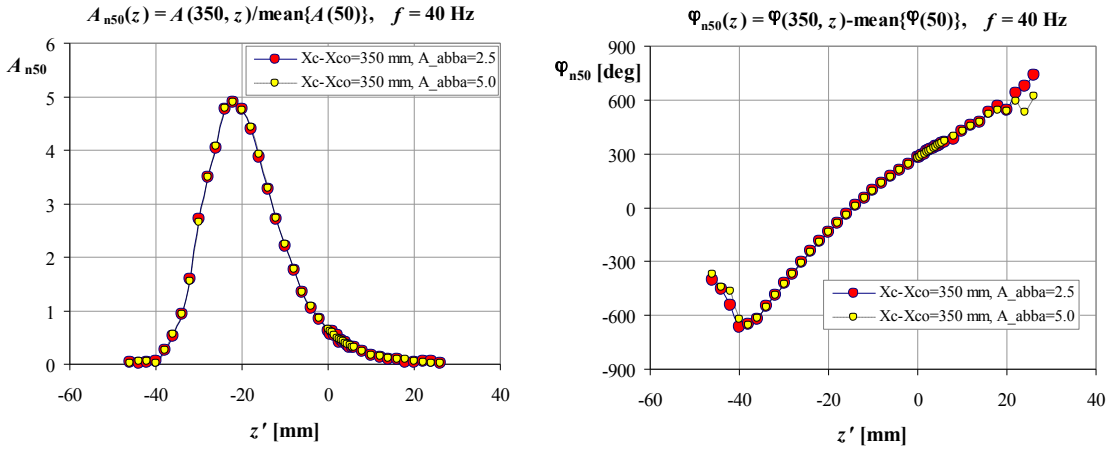

*Figure 21: Spanwise distributions of disturbance amplitudes (*left*) and phases (*right*) measured in stability experiments 'A' at* x'_s *= 399.6 mm for two amplitudes of excitation of membrane # 13 normalized by mean values measured at initial section* x'_s *= 170.9 mm.* f_{sur} *= 40.0 Hz,* A_{abba} *= 5 and 2.5.*

At the next step of data processing, the spectral phases and logarithms of spectral amplitudes of every spectral mode were approximated and extrapolated upstream to the centre of the surface nonuniformity in order to obtain estimates of initial spectral amplitudes of the excited CF-instability modes. Basically, the so-called PaL-procedure (Parabola-Line) was used. The approximation was performed for logarithms of spectral amplitudes and for spectral phases by parabolas, while the upstream approximation was carried out with straight lines, which inclinations corresponded to a parabolic derivatives taken at the first measured point. This procedure is illustrated in Figure 22 for the case of regime *5* for a fixed value of the spanwise wavenumber $\beta' = 0.576$ rad/mm. It was applied hundreds of times for all regimes and frequency-wavenumber modes under study. Such procedure was used previously in several investigations. The application of the PaL-procedure represented an optimal way of estimation of the initial values of spectral amplitudes and phases of the excited CF-instability modes based purely on the experimental data.

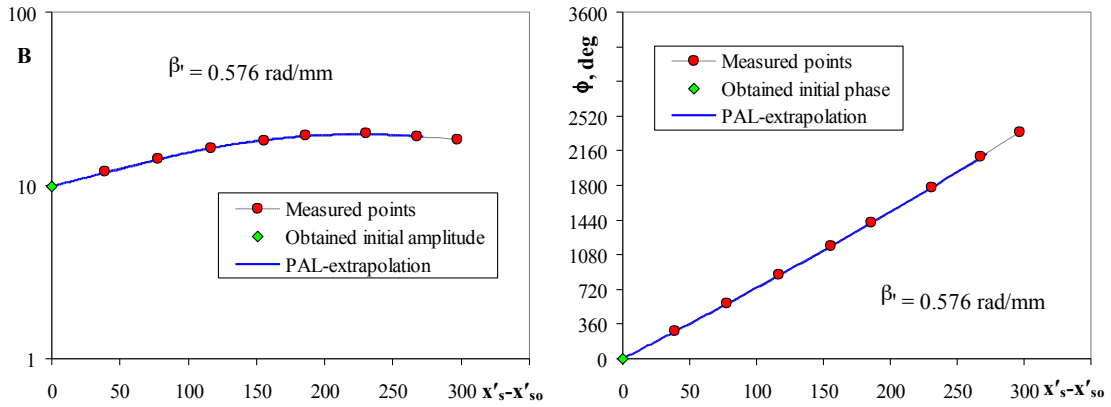

*Figure 22: Illustration of application of PAL-procedure of extrapolation of spectral amplitudes (*left*) and spectral phases (*right*) of CF-instability modes to position of centre of surface nonuniformity* $x'_s = x'_{so}$ *for disturbance excited directly by surface vibrations in receptivity experiments 'A' in regime* 5 *(*f_{sur} *= 80 Hz,* β' *= 0.576 rad/mm).*

Finally, the amplitudes and phases of the receptivity coefficients corresponding to excitation of CF-modes due to surface nonuniformities and due to scattering of freestream vortices on surface nonuniformities have been obtained. The coefficients of the boundary-layer receptivity to *surface nonuniformities* are defined as ratios of initial spectra of CF-waves and resonant spectra of surface vibrations [60]. Two examples of such receptivity coefficients are shown in Figure 23 versus spanwise wavenumber β' for regimes *5* and *2*. Note that the character of these distributions and the values of the receptivity coefficients' amplitudes and phases are close to those found in previous experiments for

the 25-degree model of a swept wing simulated by a swept plate. It is seen that the distributions are very similar to each other, as it should be, because the surface source frequencies in these two regimes are very close to each other (f_{sur} = 80 and 85 Hz). The amplitudes of coefficients of the boundary-layer receptivity to surface nonuniformities decay with the spanwise wavenumber, while their phases remain practically constant.

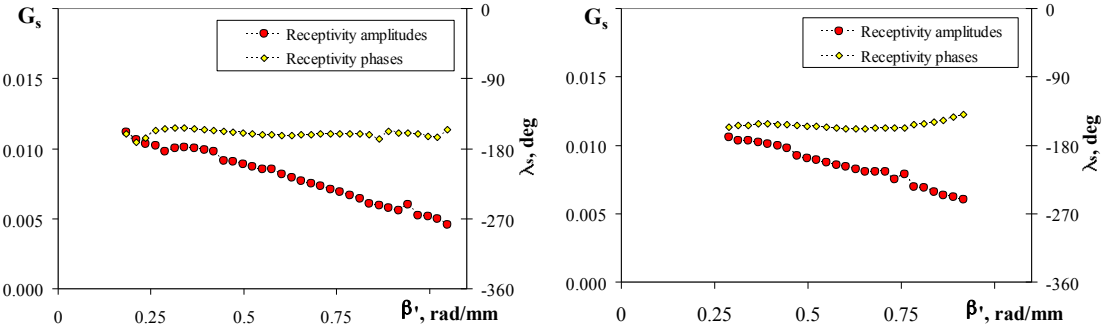

Figure 23: Amplitudes and phases of receptivity coefficients for excitation of CF-modes by surface nonuniformities measured in regimes 5 (f_{sur} = 80 Hz, left*) and 2 (f_{sur} = 85 Hz,* right*).*

Finally, the amplitudes and phases of the complex-valued receptivity coefficients corresponding to excitation of CF-modes due to scattering of freestream vortices on surface vibrations have been obtained in receptivity experiments 'A' as complex initial spectra of CF-waves divided by product of complex-valued resonant spectra of surface vibrations and complex amplitude of free-stream vortices measured at the boundary-layer edge above the surface nonuniformity. Two examples of such receptivity coefficients obtained in regimes *5* and *2* at difference frequencies f_{CF-} = 15 and 45 Hz are shown in Figure 24 versus spanwise wavenumber β′. Similar results are obtained in all other studied regimes. It is seen that, in contrast to the surface receptivity coefficients (Figure 23), the surface-vortex receptivity amplitudes and phases estimated at difference frequency differ from each other in regimes *5* and *2*. We assume that the accuracy of their estimation can be improved by means of extrapolation of the measured streamwise distributions of disturbance amplitudes and phases by the corresponding theoretical distributions. Such additional data processing is performing at present.

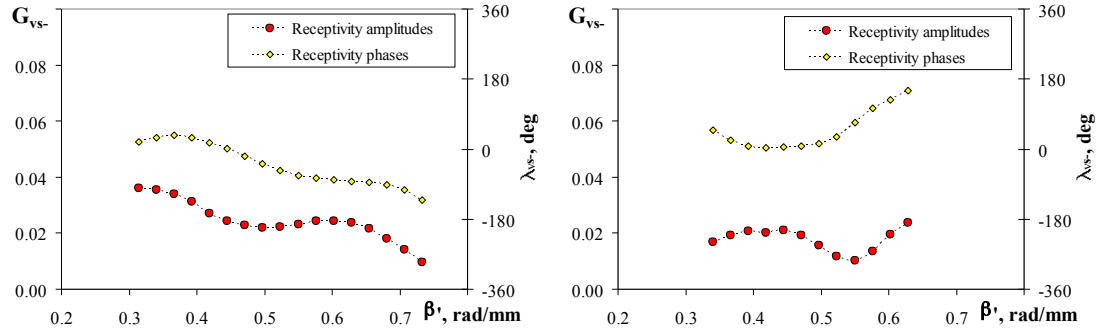

Figure 24: Amplitudes and phases of receptivity coefficients for excitation of CF-modes at difference frequency due to scattering of freestream vortices on surface nonuniformities measured in regimes 5 (f_{CF-} = 15 Hz, left*) and 2 (f_{CF-} = 45 Hz,* right*).*

4.3 Experiments B: excitation of TS-waves

The experiments devoted to study of excitation and development of unsteady (in general) TS-instability modes in the swept-airfoil boundary layer have been performed successfully at AoA of +1.5 degree, i.e. at the conditions of experiments 'B'. Similar to the experiments 'A', described above, they consisted of two main stages: (i) the TS-instability measurements and (ii) the boundary-layer receptivity measurements for the case of excitation of 3D (in general) TS-instability modes.

In Figure 25 the setup of the experiment B is shown.

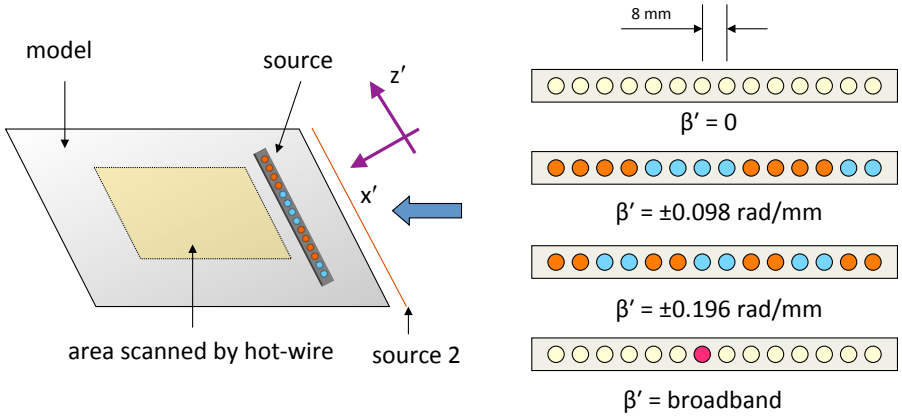

Figure 25: The setup of experiment B.

Examples of the results of the base-flow measurements, performed in experiments 'B' inside the boundary layer, are illustrated in Figure 26, where the wall-normal mean-velocity profiles are presented in dimensionless coordinates for various values of the chordwise and spanwise coordinate. The chordwise coordinate was varied in the measurements between x_n = 120 mm (the location of the surface disturbance source) and x_n = 448 mm (downstream from the end of the region of all stability and receptivity measurements. Three values of the spanwise coordinate were investigated: $z'_c = -60$, 0, and +60 mm. This range covers completely the spanwise regions of both the instability and receptivity measurements in experiments 'B'. The comparison of the measured profiles with the calculated ones shows a very good agreement. Note that the agreement is also observed with the theoretical Blasius profile (not shown). This agreement is associated with weakness of the streamwise pressure gradient in base flow in experiment 'B'. This result indicates, in particular, that the boundary-layer flow under study in experiments 'B' is spanwise uniform within accuracy of measurements and corresponds to an infinite-span swept wing.

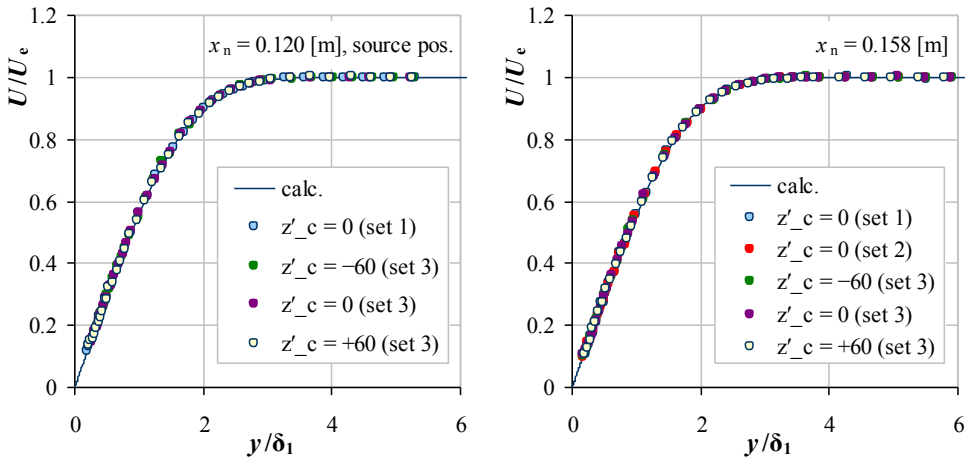

Figure 26: Wall-normal profiles of streamwise (U) component of mean-velocity vector, measured in experiments 'B' at two chordwise locations close to disturbance source (x_n = 120 and 158 mm) and three spanwise locations, shown in comparison with the corresponding calculated boundary-layer profiles.

Figure 27 displays streamwise variation of the boundary-layer integral parameters (averaged in span): (i) the displacement thickness δ_1, (ii) the momentum thickness δ_2, and (iii) the shape factor $H = \delta_1/\delta_2$, measured experimentally and calculated for the conditions of experiments 'B'. All calculated values are seen to agree very well with the measured ones. The shape factor H is almost constant in the flow under study and equals in average to 2.558 that is extremely close to the calculated shape factor averaged in the region of measurements 2.561, as well as to the Blasius value of 2.591, which is reached at $x_n \approx 420$ mm for both the measured and calculated values.

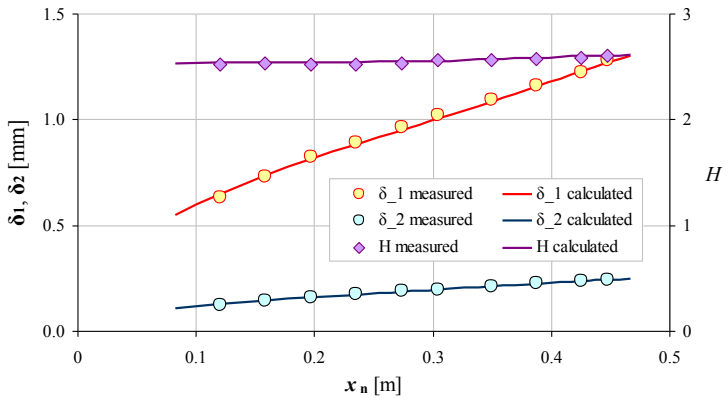

Figure 27: Measured and calculated streamwise distributions of integral boundary-layer parameters. Experiment 'B'.

During the instability measurements 'B' the 3D (in general) TS-waves were generated by the same surface disturbance source as that used in the stability experiments 'A'. The excited time-periodic perturbations were either spanwise periodic, when all membranes of the source were activated, or spanwise localized ones, when only one membrane oscillated. In the latter case the spanwise wavenumber spectrum of the excited TS-waves was broadband while in the former case only two modes (with spanwise wavenumbers ±β) were excited. In Figure 28 the measured amplitude and spectrum of TS wave train are shown.

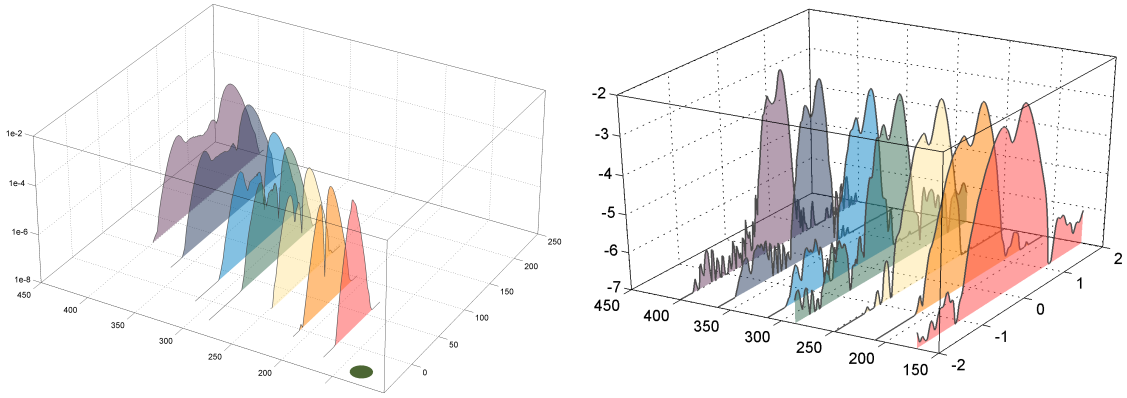

Figure 28: Amplitude of disturbances in (x′,z′) plane ploted in logarithmic scale (left) and wavenumber spectrum B(z′,β′) in logarithmic scale (right).

The amplitudes and phases of the receptivity coefficients corresponding to excitation of TS-modes due to surface nonuniformities and due to scattering of freestream vortices on surface nonuniformities have been obtained. Based on the measured data the receptivity coefficients are computed. Two examples of such receptivity coefficients are shown in Figure 29 versus spanwise wavenumber β′. Note that the character of these distributions and the values of the receptivity coefficients' amplitudes and phases are somewhat lower than those found in previous experiments for the Blasius boundary layer, although the shapes of the distributions are similar: the receptivity amplitudes increase with absolute value of the spanwise wavenumber, while the receptivity phases change very little. It is seen also that the distributions shown in Figure 29 are very similar to each other, as it should be, because the surface source frequencies in these two regimes are rather close to each other (f_{sur} = 221 and 255 Hz). This results display a good repeatability of the obtained results.

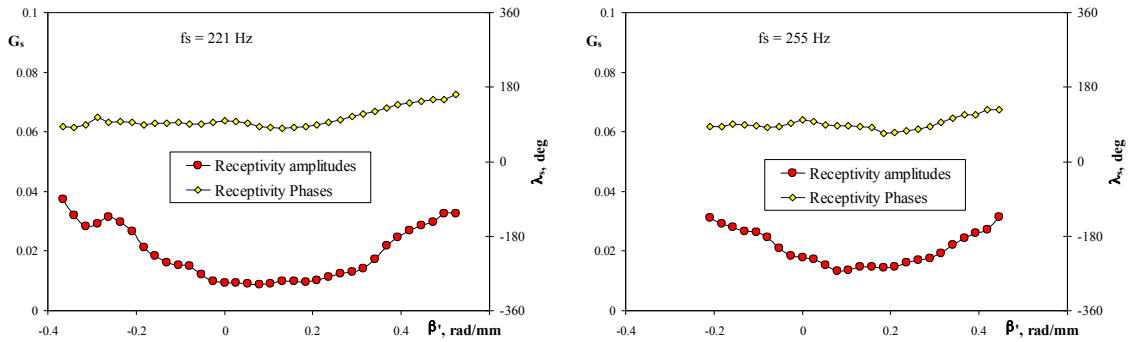

Figure 29: Amplitudes and phases of receptivity coefficients for excitation of TS-modes by surface nonuniformities measured in regimes 1 *(*f_{sur} *= 221 Hz,* left*) and* 2 *(*f_{sur} *= 255 Hz,* right*).*

4.4 Experiments C: nonlinear surface-roughness receptivity and transition

In this task the critical size of discrete roughness elements, where transition is directly triggered behind the roughness, is experimentally investigated. Here, infrared (IR) and hot-wire measurements were performed to determine transition behind a single roughness element placed near the leading edge of a 35 degree swept airfoil at negative (-5 degrees) angle of attack with the rotation axis parallel to the leading edge. A negative angle of attack decreases the sensitivity to Tollmien-Schlichting wave-type instabilities and instead makes the boundary layer flow mainly sensitive to cross-flow instability disturbances.

The sizes of roughness elements were chosen based on analysis performed by AIRBUS. Based on the pressure distribution of the RECEPT geometry, boundary-layer computations were performed. Using the characteristics of the boundary layer at different freestream speeds, the critical size of the roughness elements and steps were computed (see Figure 30).

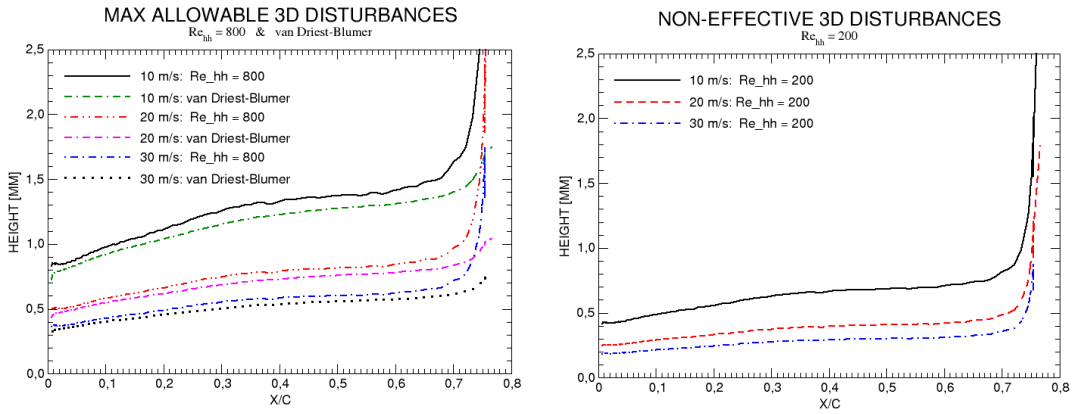

Figure 30: Maximum allowable height (left) and height of non-effective (right) of 3D roughness elements as a function of their streamwise location.

The airfoil was heated by blowing air through its hollow structure and transition was detected through infrared temperature measurements of the airfoil surface. The physical background behind the detection method is that if transition occurs, the flow at the wall inside the turbulent wedge behind the roughness element will have a larger friction than the laminar flow outside and hence a larger heat transfer, making the wall temperature lower in this region.

Several different parameters of the roughness elements were investigated, such as the diameters (8, 16 and 32 mm) and heights (200, 400 and 800 micron) of the roughness elements as well as (upstream) free-stream velocities (9–27 m/s) and turbulence levels (0.03, 0.3 and 0.8 %) of the approaching flow. Figure 31 shows the roughness elements with different size placed on the wing model.

Figure 31: The three different diameters roughness elements (i.e. D =8, 16 and 32 mm) placed on the wing. Note that the centre of the roughness element is the same for all three sizes. Flow is from right to left.

An example of the IR measurements is depicted in Figure 32.

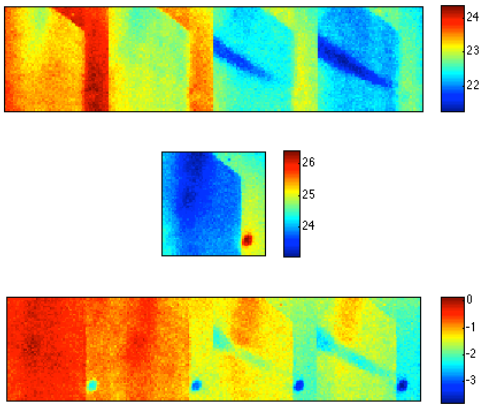

Figure 32: Example of IR measurements for roughness element with diameter and height of 16 mm and 400 micron under a free stream turbulence level of 0.3 %. Top: raw images, Middle: background level, Bottom: "raw image"-"background level". From left to right: 9, 18, 23 and 27 m/s.

Additionally to the IR measurements, hot-wire measurements within the boundary layer have been performed to ascertain the interpretation of the IR images. As apparent from Figure 34, the results for roughness heights of 400 micron showed the richest spectrum of flow regimes and it was therefore decided to focus on this particular roughness dimension. An exemplarily result from the hot-wire measurements is given in Figure 33, where the results from the IR measurements presented in Figure 32 could be confirmed through a spanwise scan within the boundary layer as apparent from the time-series, probability density function and spectra of the streamwise velocity component.

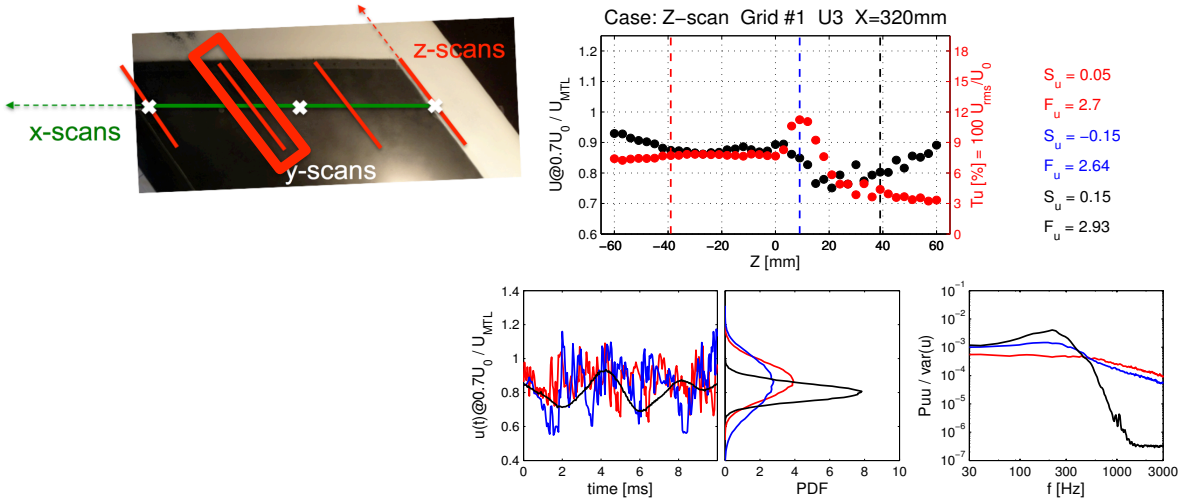

Figure 33: Example of the boundary layer hot-wire measurements for the same roughness element dimensions and flow case as in Figure 32. The streamwise velocity measurements are performed within the boundary layer at a location where the mean velocity is 70% of that at the boundary layer edge. Top left:

Photograph with coordinate system and the location of the spanwise scan (thick red box). Top right: Mean and turbulence intensity in spanwise direction. Bottom left: Excerpt of the time trace including PDF at three selected spanwise locations. Bottom right: Streamwise spectra for the three selected locations.

The results of all measurements are summarized in Figure 34.

R-E height [µm]	Grid #: / Speed U_{MTE} [m/s]	0 (Tu =0.03%)			1 (Tu =0.3%)			2 (Tu =0.8%)			Re_{hh} $U_h h/\nu$
200	9	8	16	32	8	16	32				140
	18	8	16	32	8	16	32				280
	27	8	16	32	8	16	32	8	16	32	420
400	9	8	16	32	8	16	32	8	16	32	280
	15								16		480
	17	8									540
	18	8	16	32	8	16	32	8	16	32	570
	22		16			16					700
	27	8	16	32	8	16	32	8	16	32	850
800	9	8	16	32	8	16	32				570
	18	8	16	32	8	16	32				1150
	27	8	16	32	8	16	32				1700

No observable effect: Slight effect: Effect: Transition:

Figure 34: Table of tests. Cases with no observable effect, a slight effect meaning that some streakiness can be seen downstream the roughness element, a clear effect but not distinct transition as well clear transition are marked with different color coding.

A summary of the measurements is given in Figure 35 where the data is presented in terms of $R_k=kU_k/\nu_k$ and ratio of the diameter to height d/k. The shaded area corresponds to correlation data from von Doenhoff & Braslow. As it can be seen there, the present set of data expands the range of available database to include higher aspect ratios of the roughness. Further, it shows that the current set of data for the three-dimensional flows fits reasonably well with the those for two-dimensional flows collected by von Doenhoff & Braslow.

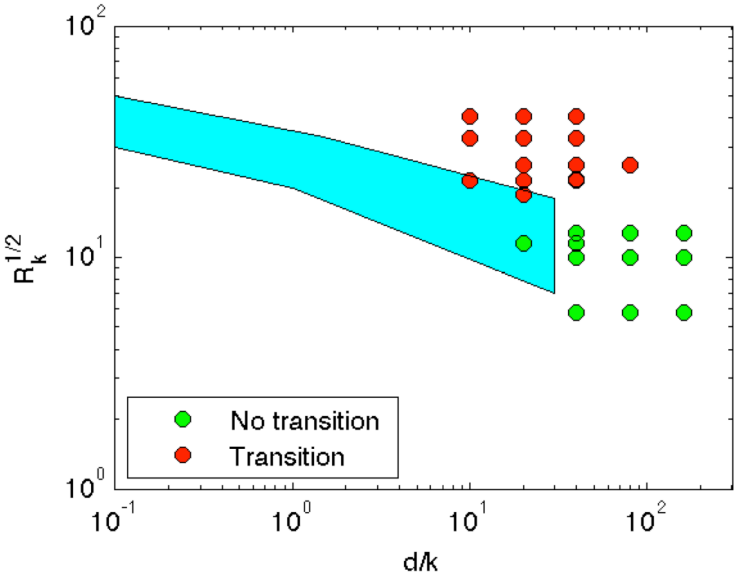

Figure 35: Summary of results from the experiments on critical roughness size. The data is presented in terms of $R_k=kU_k/\nu_k$ and ratio of the diameter to height d/k. The shaded area corresponds to correlation data from von Doenhoff & Braslow.

5 Direct numerical simulations

5.1 DNS of receptivity to medium-size roughness elements

The simulations of medium-size roughness elements in high-speed flows have been performed by group of Stuttgart University. The in-house FD/Fourier-spectral DNS-code NS3D has been adapted for numerical computations on curved surfaces of an airfoil and the algorithm to transfer baseflow data onto DNS grid has been prepared. Further, the code has been adapted for new Cray XE6 super computer.

A grid for a confined area on surface of the modified NACA67 airfoil (RECEPT geometry) has been generated and numerical behaviour on highly deformed grid around cylindrical roughness element has been studied with the focus on accuracy and CPU time. Two grid strategies are followed: immersed interface technique combined with domain decomposition (for rectangular and round roughness), and gridded roughness using coordinate transformation. A literature study on necessary resolution of roughness elements has been made. The flow parameters for the modified NACA67 airfoil at high-speed were chosen such that the Mach number based on the total velocity is less than unity to avoid shock in front of roughness elements. High-resolution baseflow simulation was performed using the DLR TAU code. This base flow is then used to define the boundary conditions in DNS simulations. To perform direct numerical simulations, grids with different roughness heights have been generated using proprietary software Gridgen.

To investigate effects of flow three-dimensionality on the structures behind the roughness elements a two-dimensional baseflow (zero sweep) using DLR-TAU code was computed. Then, DNS of flow with the roughness-element in this two-dimensional boundary layer was performed.

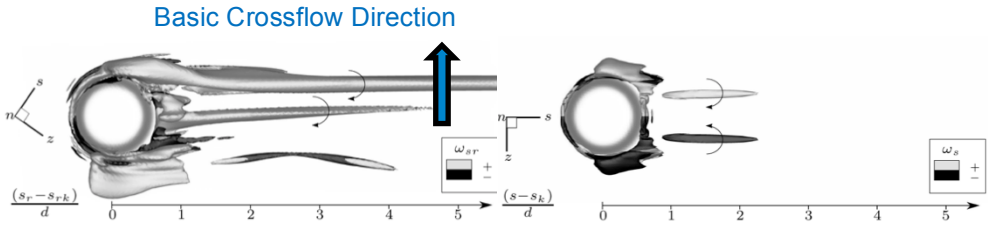

Figure 36: Comparison of vortex system behind large roughness elements in 3D (left) and 2D (right) boundary layers., λ_2= -30000, h=$\delta_{1,s}$.

Results of simulations in two- and three-dimensional flows studied here are presented in Figure 36. As can be seen there, the in two-dimensional flow case a pair of symmetric vortices are generated, while in three-dimensional flow case the flow behind the roughness element is non-symmetric.

Extended stability analysis of baseflow was performed to account for unsteady disturbance modes as preparation for the introduction of controlled disturbances in the DNS. To compute the growth rate of perturbations Fourier analysis of available DNS data has been performed.

High resolution DNS were performed with various roughness heights to narrow down the range where the element becomes transition-effective. In the present scenario with a 3D boundary layer, a successive elevation of the roughness element enhances the amplitude of the crossflow vortices, which leads to an earlier onset of secondary instability and, therefore, to premature transition. However, with the element reaching a certain height, another mechanism influences the transition process: The wake of the element becomes unstable, periodically shedding vortex structures (cf. Figure 37a). The latter unsteady structures are damped by the boundary layer, as long as the element height stays within a certain limit. Exceeding this limit results in a persisting contamination of the flow in the downstream centerline of the element, ultimately causing transition in very close proximity to the element (cf. Figure 37b-c).

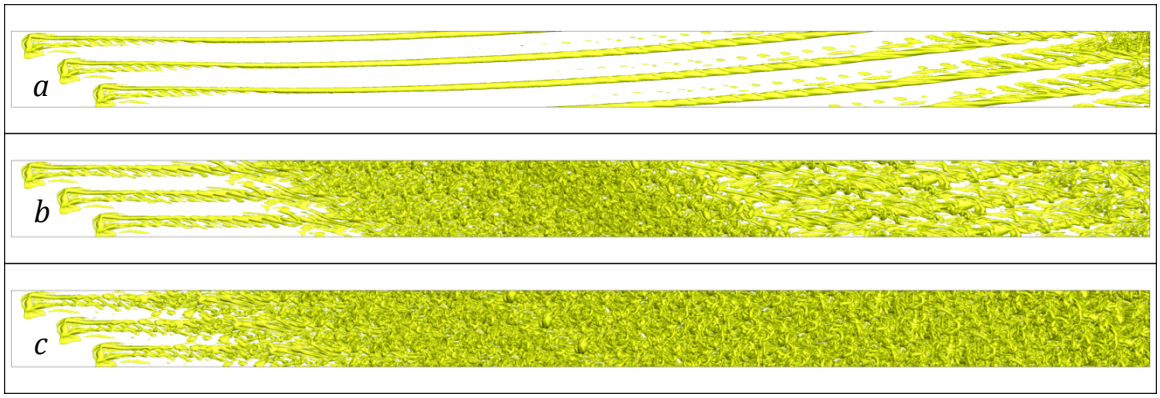

Figure 37:Vortex visualisation (isosurfaces λ_2 = -20000) for increasing roughness-element heights: a) k/δ_{1s}=1.25, b) 1.31, c) 1.38, with Re_{kk}=436, 475, 514, respectively; uncontrolled background disturbances.

Depending on the roughness height, two routes to turbulence were identified based on the simulations performed here:

- Discrete roughness elements create a horseshoe vortex, where one leg relaxes to a high-amplitude steady crossflow vortex. Secondary instability of these vortices rapidly leads to turbulent flow (see Figure 38).
- A Kelvin-Helmholtz type convective instability of the recirculation zone in the near wake leads to periodic vortex shedding. When reaching non-linear amplitudes, step (1.) is bypassed and these vortices trigger premature transition. For very high roughness elements, the near-wake behavior changes to a global instability.

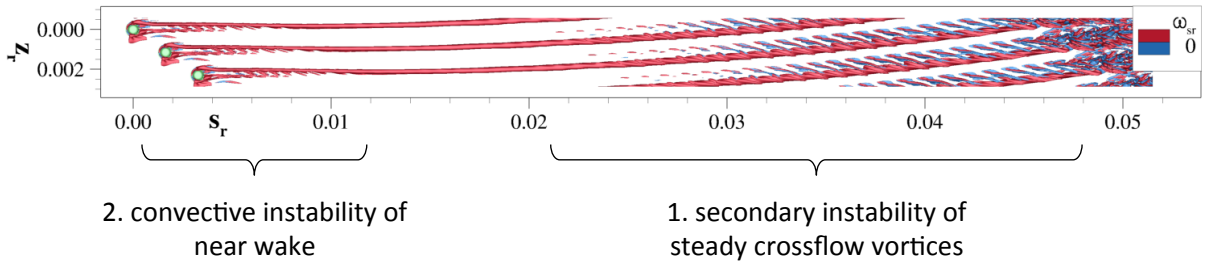

Figure 38: Flow field behind a discrete roughness element.

In performed studies also effects of background perturbations has been studied, where a realistic and a high level perturbations has been considered. It was found that an increased level of introduced disturbances can shift the effective roughness Reynolds number $Re_{kk,\mathrm{eff}}$ to smaller values, if the disturbance amplitudes in the near wake grow to a certain level. Further effects of spanwise periodicity of roughness elements are also studied.

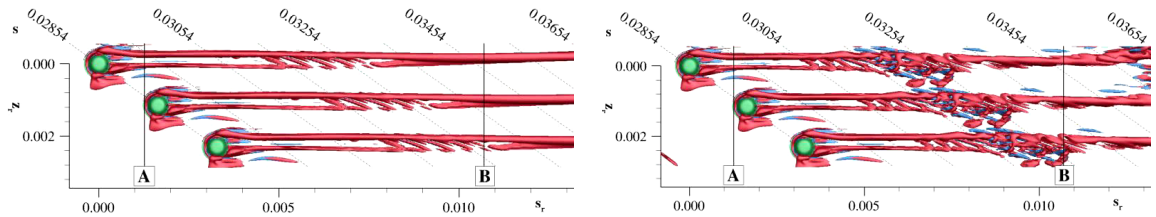

Figure 39: Effects of background noise on breakdown of vortices caused by roughness elements.. Simulations with realistic (left) and high (right) level of noise. k=1.375, Re_{kk}=487.

When the spanwise spacing of the periodic roughness elements is doubled, the near-wake behaviour is virtually unaffected in convectively unstable cases.

Cylindrical roughness elements in the investigated 3D boundary layer produce (nonlinear) wake vortices that are either damped or supported by the basic crossflow, depending on their rotational sense and thus their affinity to pure crossflow vortices. With growing roughness height, the recirculation region behind the element gains in importance regarding the evolution of the flow. Two essentially different scenarios are observed: Up to a roughness height of $k/\delta_{1,s}$=1.0, Re_{kk}= 296, a single persisting (crossflow) vortex is observed in the far wake of the element which becomes secondarily unstable within the DNS domain. In contrast, the near wake of elements with a height of $k/\delta_{1,s}$=2.0, Re_{kk}= 912, is governed by a global instability around the element. This mechanism is a changeover of the strong convective instability found for $k/\delta_{1,s}$=1.5, where steady streamwise vortices are still present behind the element and are broken up by interaction with the prevailing unsteady structures shed from the separated near-wake region.

The effective, i.e. directly flow-tripping roughness Reynolds number is in the order of 600 and is in accordance with estimations of $Re_{kk,crit}$ ranging from 325 to approximately 800 for 2D flows as summarized by Klebanoff et al.. Note that in the 3D situation here (i) the effective roughness Reynolds number is in the range of the critical roughness Reynolds number for 2D flows, the latter typically defining the boundary between completely ineffective and transition-promoting roughness, and (ii), any small roughness gives rise to exponentially amplified steady disturbances without external forcing, rendering the critical roughness Reynolds number smaller than in 2D base flows.

5.2 DNS of receptivity to small roughness elements

Here a number of different simulations have been performed to address receptivity of three-dimensional boundary-layer flow to small roughness elements. These simulations cover both low-speed (incompressible) and high-speed flows.

5.2.1 High-speed flow simulations for RECEPT geometry

Group of Stuttgart University have performed a series of direct numerical simulations of small roughness elements placed on the surface of the RECEPT geometry to compute the receptivity coefficients. The shape of the roughness elements is given by a shallow circular disc, which is smoothly blended to the undisturbed surface. The shape of the roughness element and the its corresponding Fourier spectrum are given in Figure 40.

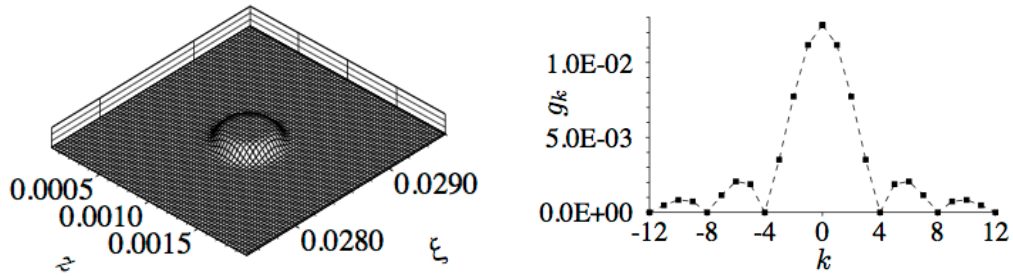

Figure 40: Shape of roughness element (left) and its discrete Fourier spectrum (right).

In the analysis performed here, both the height and aspect ratio of the roughness were varied.

Receptivity coefficients are commonly defined as the ratio of the effective disturbance response to an appropriate measure for the input amplitude. This definition corresponds to the linearised receptivity theory for the excitation of crossflow instabilities by localised surface roughness. For the receptivity coefficient, we transform the velocity components to an edge-streamline oriented coordinate system, normalise the results by the magnitude of the local base-flow edge-velocity, and take the wall-normal disturbance maximum of fundamental mode. The initial disturbance amplitude right at the roughness can not be determined directly, but can be reconstructed by matching an N-factor curve for the

respective mode to the DNS result at a reference point, where near-wake effects have decayed. This procedure implies exponential growth behaviour and is valid for amplitudes at reference point not much larger than about 0.01. Summary of some results are given in Figure 41.

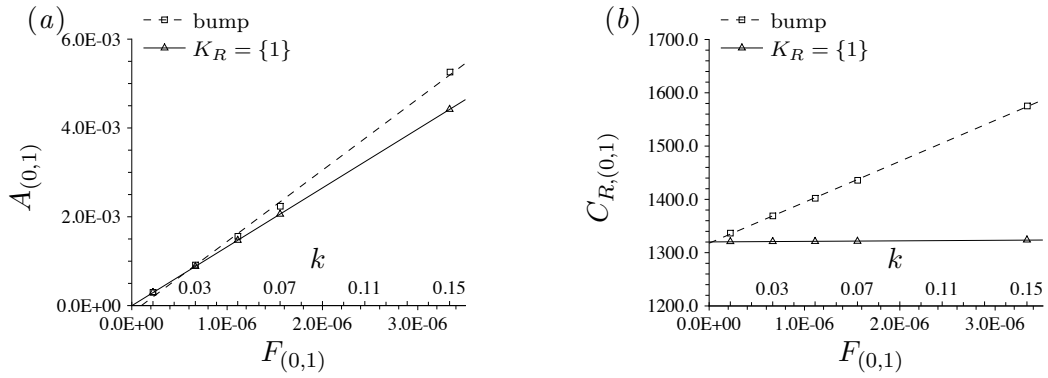

Figure 41: Receptivity amplitudes (a) and receptivity coefficients (b) for mode (0,1), for bump elements and spectrally reduced elements, heights k = 0.01/0.03/0.05/0.07/0.15. Symbols: DNS results. Lines: linear curve fits.

Motivation of performed analysis was recent experimental and numerical results concluded to show a linear increase in the amplitudes of steady crossflow modes with the height of those elements at constant diameter. However it turns out that the amplitude of the most amplified steady crossflow mode at a reference station downstream clearly scales super- linearly with the element height at constant diameter, as predicted by theoretical results based on large-Reynolds-number asymptotic theory. The position of the reference station excludes ongoing transient growth effects. Thus the receptivity coefficient is not a constant, rather a linear function of the roughness modal amplitude in this situation; this holds for element heights up to at least 30% of the local displacement thickness at the considered Reynolds number $Re_{\delta 1,s}$ = 500. Only for roughness shapes that consist of alternating bumps and dimples of equal shape and size, and thus have zero spanwise mean, a constant receptivity coefficient is found. However a zero spanwise mean of the shape is not sufficient: If the spanwise bump/dimple structure has differing heights and depths but still zero spanwise mean, receptivity is again non-linear. Evidently, the "flow blockage" is decisive, scaling non-linearly with the roughness height (or depth) due to the wall-normal gradient of the streamwise velocity: Whenever the spanwise mean of the blockage is non-zero, receptivity is non-linear. For increasing the element height at constant aspect ratio, the super-linearity is virtually negligible; recent theoretical results by Luchini (2013), suggesting that the super-linearity is closely connected to the changing aspect ratio with increasing element height, are therefore confirmed. For high elements it is known that the roughness Reynolds number Re_{kk}, based on the variables taken at the roughness height in the undisturbed boundary layer, is a meaningful parameter, and this approximately scales quadratically with the roughness height k. This quadratic influence basically exists already at small heights but is not yet dominating in this "linear" regime.

A series of simulations were performed modeling the roughness elements through inhomogeneous boundary conditions. The applicability of inhomogeneous boundary conditions as a means to model discrete roughness elements is limited to small roughness elements, however the upper boundary is still to be determined. The receptivity behaviour for larger bump elements up to $k/\delta_{1,s}$= 0.30 is depicted in Figure 42 for the meshed case and the Taylor case. For larger elements, our method to reproduce the receptivity amplitudes at the roughness elements is not valid anymore due to non-linear saturation of mode (0,1), further the flow in close proximity to the element starts to differ qualitatively between meshed and modelled roughness. In the considered range, the receptivity amplitudes $A_{(0,1)}$ obtained

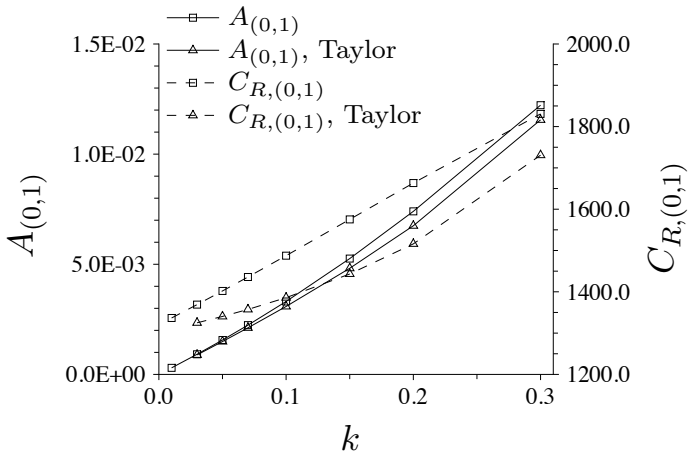

Figure 42: Receptivity amplitudes and coefficients for mode (0,1), meshed and modelled bumps. Symbols: DNS results.

5.2.2 *Incompressible flow simulations for ONERA D & DTP-B geometry*

In beginning of the project a delay in start of experimrntal work was foreseen and Onera chose to perform studies on the so-called DTP-B profile which has been largely studied experimentally (F2 onera wind tunnel) and by instability approaches. The chord is 0.7m, the span 2.5m, the sweep angle 40°, the incoming velocity 70 m/s and the chosen angle of attack -6°.

The first activity was the computation of the main flow around the profile. Using the in-house Onera code elsA.

To perform direct numerical simulations of flow over DTP-B airfoil, with or without roughness element, a high-resolution structured grid (453x155x209) has been generated. First, simulations without roughness elements have been performed to create the mean flow and check the quality of the grid. The obtained pressure coefficient is in good agreement with the experimental data. Simulations with roughness elements have been then prepared (Figure 43). After several unsuccessful attempts it appeared clear that some specific and important improvements especially for the numerical schemes close to the wall were necessary.

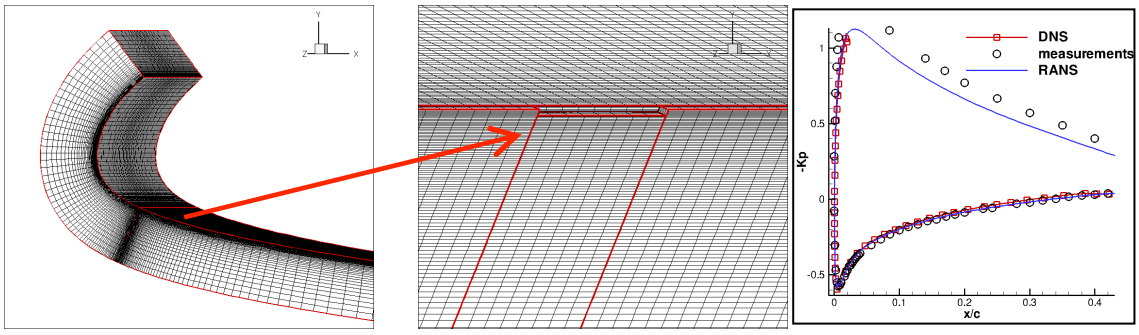

Figure 43: Computational grid for direct numerical simulations of flow over DTP-B geometry in presence of roughness element (left and middle). Computed pressure coefficient (right).

This strong intervention has been thus performed. However in order to check the new elsA code, it has been decided as a first step to consider the Poll's cylinder test case in the receptivity condition which has been calculated by Estelle Piot in her doctoral work and furthermore using the same mesh. It must be recalled that Estelle Piot used another code (Funk code, also developed at Onera). This one is very accurate but cannot be easily adapted with the same accuracy to non-regular geometries. As planned in subtask 2.1 of the present project, this case deals with the receptivity induced by an array of micron-sized roughness elements which are regularly spaced in the spanwise direction. These roughness elements are placed on the neutral curve. In case of Poll's cylinder, the geometry is a cylinder with a radius of 10 cm placed in a flow with an incoming velocity of 50 m/s and a swept angle of 60°. The

size of the roughness element corresponds to 1/10th of the local boundary layer height and is in the upper limit of the expected linear receptivity mechanism.

After significant modifications in the elsA code, interesting results have been finally obtained, firstly in this academic configuration corresponding to Poll's cylinder. In order to make sure that the two-dimensional DNS solution is correct, the velocity profiles are compared with the boundary-layer solutions from 3C3D code and the RANS solution interpolated on the two-dimensional DNS mesh. From the Figure 44 it may be concluded that the DNS computation catches correctly the boundary layer, even better than the RANS computation.

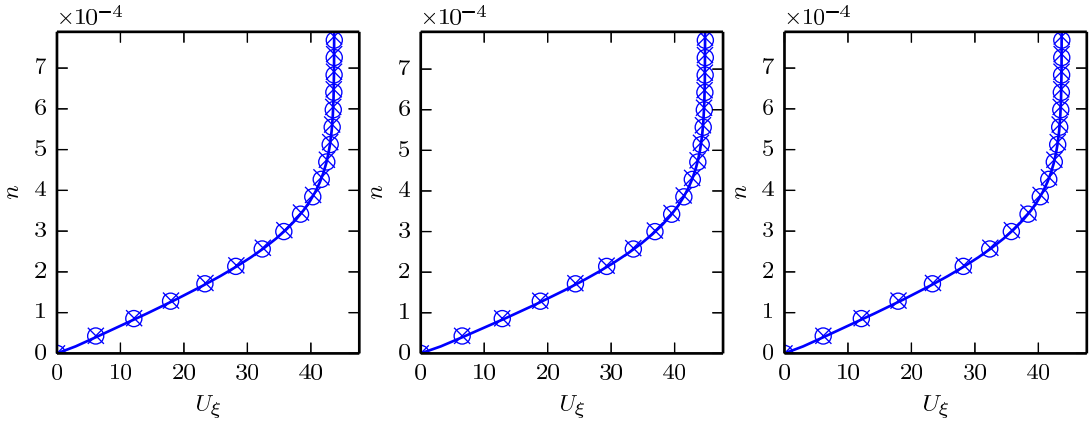

Figure 44: Comparison of the streamwise velocity profiles U_ξ (m/s) versus the wall normal location n (m) at three different streamwise positions obtained by means of DNS computation (solid line) and 3C3D solver where the velocity field at the boundary-layer edge is either extracted from the DNS computation (x) or computed from RANS solution wall pressure (o).

In Figure 45 the amplitude of perturbation from DNS is compared to those from stability calculations based on different meanflow fields. These fields are obtained from:

(A) 3C3D boundary-layer computations based on analytical potential flow as edge velocity,

(B) 3C3D boundary-layer computations based on edge velocity distributions extracted from the mean value of the three-dimensional DNS solution,

(C) The boundary layer directly extracted from DNS.

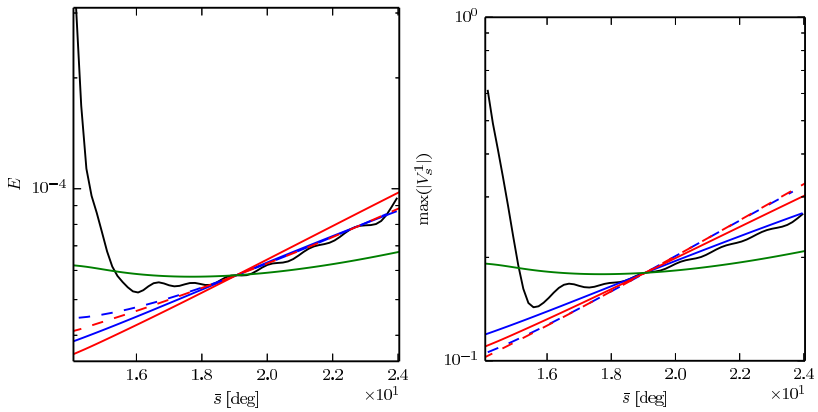

Figure 45: Crossflow wave amplitudes extracted from DNS based on the energy E and maximum of streamwise velocity. Results of local (solid curves) and nonlocal (dashed curves) linear stability analysis of meanflows A (blue), B (red) and C (green).

The agreement is good and similar to the computations by Piot. After a transient phase, the amplification is in excellent agreement with linear stability theory. As far as local stability theory is concerned, it is interesting that the base-flow leading to the best agreement between the DNS solution and local stability theory depends on the norm. As matter of fact, an excellent agreement is observed between the DNS solution and base-flow C on the amplitudes evolution based on maximum of

streamwise perturbation velocity. However, on the three other curves the best agreement is obtained with base-flow A.

However, when the ONERA DTP-B geometry was analysed again, the results were not satisfactory. Despite extensive investigations, the computed flow field showed poor agreement with boundary-layer computations. Therefore, It was decided to concentrate the effort on another geometry. For that purpose the ONERA-D profile was chosen, since there is a long experience of simulations for that geometry. The performed RANS simulations show a good agreement with the boundary-layer computations. Extensive studies on grid convergence for DNS and effects of boundary conditions are performed and a finally the grid and boundary conditions with satisfactory results are found. These are chosen for simulations of receptivity to roughness elements. For simplicity, in these simulations the attachment line is excluded from the computational domain. It has been shown that DNS result matches very well results of boundary layer equations solver (see Figure 46).

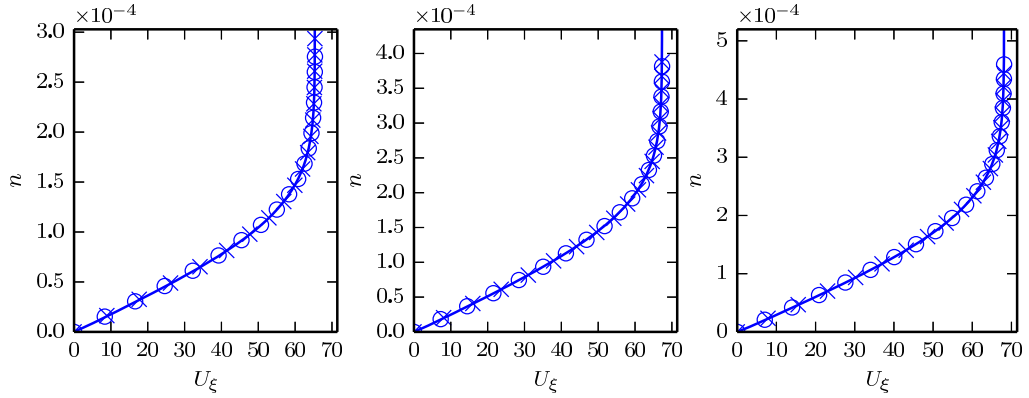

Figure 46: Comparison of the streamwise velocity profiles U_ξ (m/s) versus the wall normal location n (m) at three different streamwise positions obtained by means of DNS computation (solid line) and 3C3D solver where the velocity field at the boundary-layer edge is either extracted from the DNS computation (x) or computed from RANS solution wall pressure (o).

The perturbation field is computes as the Figure 47 (left) gives the axial component of the perturbation velocity at a distance of 0.375δ from the wall. These structures are similar to crossflow modes. Perturbation profiles agree well with result of the nonlocal linear stability theory, showing that the correct crossflow wave has been captured by elsA DNS. However, the amplitude of perturbation in DNS decays along the streamwise direction, while an amplified wave was expected. Moreover, although the stretched mesh in the buffer domain leads first to perturbation damping, a quite strong perturbation is observed at the end of the computational domain. This phenomenon is not understood yet and its effect on the development of crossflow waves is unknown.

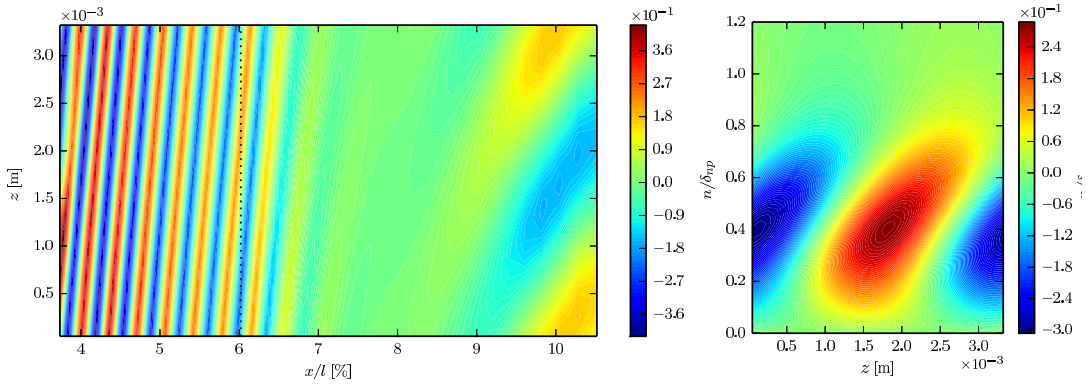

Figure 47: Streamwise velocity component of the perturbation in x-z plane at normal position n = 0.375δ (left) and z-y plane (right).

This study has shown the ability of elsA DNS (usually used for aeroacoustics simulations) to handle receptivity computations. A specific numerical methodology was settled. In future, elsA DNS might

be used with confidence on more refined mesh to catch the exact initial amplitude of the stationary crossflow wave generated by roughness element of different sizes.

5.2.3 *Incompressible flow simulations for NLF(2)-0415 geometry*

KTH and FOI have performed simulations to examine disturbance evolution and control of the boundary-layer flow over a swept wing (NLF(2)-0415) mounted in a wind tunnel at an angle of attack of -4^o. Note that the angle of attack is defined in a plane normal to the leading edge. The sweep angle is 45^o. The wing geometry is invariant in the spanwise direction as is the resulting boundary-layer flow. This configuration favours the growth of crossflow disturbances because of a strong favourable pressure gradient on the upper wing side. The geometry is shown in Figure 48.

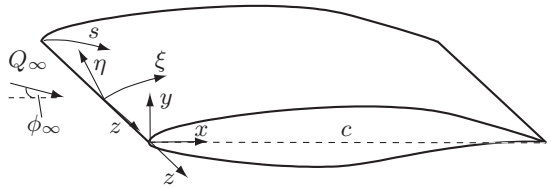

Figure 48: Swept NLF(2)-415 wing, with sweep angle of 45º. The angle of incident flow is –4º.

This flow configuration conforms to experiments by Saric et al. (1998a) who excited crossflow disturbances which were aimed at nonlinearly stabilising the boundary layer. These were generated in a controlled manner by placing a spanwise array of micron- sized roughness elements close to the leading edge. The roughness elements were placed at x/c = 0.023 with a spacing of 8mm. Direct numerical simulations were performed using the nek5000 code by Fischer et al. (2008). RANS simulations of the model placed inside the wind tunnel were performed. The results of these simulations were used to define the boundary conditions for DNS of flow over the wing.

The natural surface roughness with an r.m.s. value of 0.65μm was modeled by by inhomogeneous boundary conditions. We thus project the zero-slip condition on the surface of the roughness to the smooth undisturbed wall. The cylindrical roughness elements used to excite the control mode on the other hand are inserted into the computational grid by displacing the respective grid nodes at the wall. Their chordwise position is chosen as x_r/c = 0.025, i.e. close to the experimental position, while the height is 15.6μm (see Figure 49). The results of DNS were compared to nonlinear nonlocal stability analysis performed with NoLoT/PSE code.

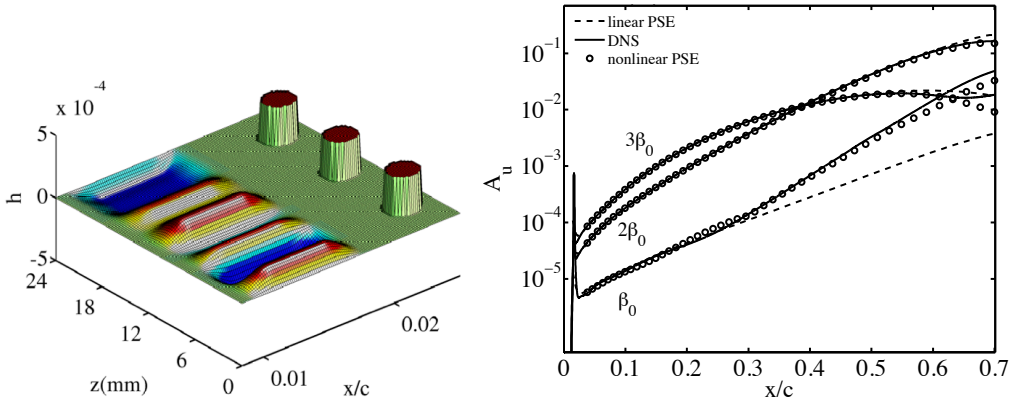

Figure 49: Left: Geometry of roughness used in simulation. Right: Comparison of amplitude of crossflow vortices obtained from DNS and nonlinear nonlocal stability computations (PSE) for the uncontrolled case.

In order to trigger the transition in DNS, a random volume forcing inside the boundary layer was applied. The amplitude of the random forcing was chosen such as to obtain transition at x/c ≈ 0.5, i.e. significantly upstream of the experimental transition location. The present flow thus exhibits unsteady

disturbances of higher amplitude as compared with the experiments and allows evaluating the robustness of the control. The plots in Figure 50 represent two cases were in one case the transition is casused by crossflow instabilities (left), while in the other case (right) transition is delayed with placing control roughness elements near the leading edge damping stationary crossflow vortices. These simulations showed that for the case studied here micron-sized roughness elements are a very efficient means of transition control.

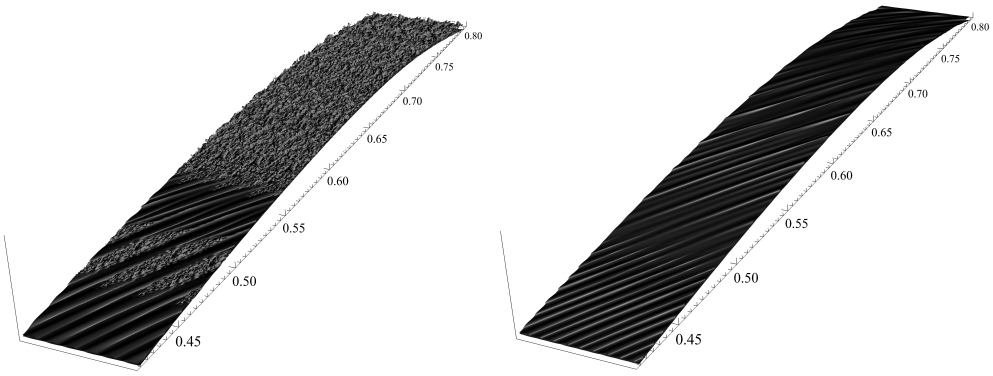

Figure 50: DNS of transition caused by crossflow instabilities (left), transition delayed by placing control roughness elements near the leading edge (right).

In order to understand the physics of the observed behavior, amplitude of different Fourier component of the flow filed was computed. A rather complex disturbance environment becomes apparent in Figure 51(a), where the natural case is presented. Both steady and unsteady disturbances are present and grow almost within the entire domain. The low-frequency disturbances are found to be of similar order as the steady disturbances in the uncontrolled case or even to exhibit higher amplitudes. At the position marked in figure 5(a), which is located just upstream of transition, high-frequency disturbances undergo sudden amplification and finally attain amplitudes that are of similar order as compared with the steady and low-frequency instabilities. This is consistent with experimental observations (cf. Deyhle & Bippes 1996; White & Saric 2005) as well as theoretical and numerical studies (Malik et al. 1999; Wassermann & Kloker 2002, 2003) and points to the emergence of secondary instabilities. The situation is different in the controlled case. The respective amplitudes are depicted in Figure 51 (b). The steady disturbances are clearly dominant. Their initial spatial evolution corresponds well to that of the control mode. Hence, the control mode excited by the circular roughness cylinders seems to dominate the disturbance field for $x/c < 0.5$. It is apparent that those low-frequency disturbances which are dominant in the natural case are attenuated. Furthermore, the sudden growth of high-frequency disturbances prior to transition is shifted downstream, corresponding to the transition location for the controlled case. The control has successfully weakened the growth of secondary instabilities. This observation confirms results by Wassermann & Kloker (2002), who found that this kind of control leads to a three-dimensional flow state that attenuates the growth of high-frequency secondary instabilities. In particular, they found the control mode to decrease regions of deceleration of the steady flow nonlinearly. A strong region of deceleration is known to favour the growth of secondary instabilities.

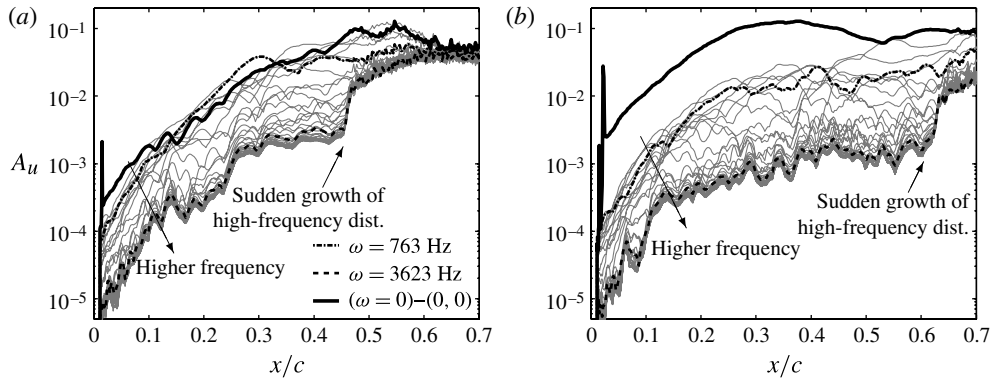

Figure 51: Amplitude evolution of steady and unsteady disturbances for (a) the natural case and (b) the controlled case. The grey lines represent unsteady disturbances plotted at a constant frequency step size (190 Hz).

Here, it was demonstrated that, upon exciting the steady control mode, transition is completely suppressed within the computational box. It is shown that both the most unstable unsteady primary disturbances and high-frequency secondary instabilities are attenuated when control is employed. The characteristic sudden growth of high-frequency secondary instabilities prior to transition is completely suppressed. So far the control approach studied herein has only been used for boundary-layers where transition was induced by stationary crossflow disturbances. It was demonstrated that the control is robust. It effectively suppresses transition which is induced by a complex disturbance field involving both steady and unsteady primary crossflow disturbances.

5.3 DNS of receptivity to free-stream vortical disturbances

5.3.1 High-speed flow simulations

To study the receptivity to free-stream perturbations direct numerical simulations of the flow over the modified NACA 67 airfoil (RECEPT geometry) including the leading edge has been performed by group of Stuttgart Universiy. The freestream incides with an angle of attack of -6.1^{o} and a sweep angle of 35^{o}. Steady base flows are computed with the Reynolds-Averaged Navier-Stokes (RANS) solver TAU, developed by the German Aerospace Center (DLR); the setup is illustrated in Figure 52. Two free-stream conditions are chosen for the present investigations giving freestream Mach numbers of 0.16 and 0.65.

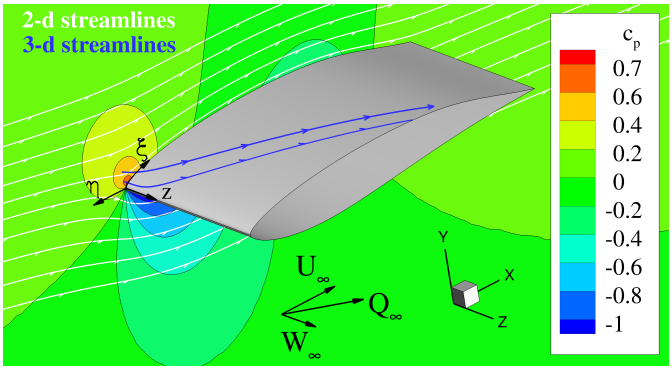

Figure 52: Setup of the infinite swept wing for the RANS base flow computation, with contours of the pressure coefficient cp, based on the high-speed case data. 2-d streamlines are plotted by setting the spanwise velocity component to zero. 3-d streamlines start in the stagnation line region close to the surface.

DNS are performed with our block-structured, 6th-order accurate finite-difference code NS3D. Due to the different boundary-layer thick- nesses, an appropriately structured grid has been generated for each

case. Both computational domains enclose the leading edge and a small part of the lower wing side; the inflow boundaries are identical. The upper-side extent for the high-speed case covers a range up to $x = 0.08$, see Figure 53, whereas the low-speed-case setup ends at $x = 0.20$. The grids are augmented by stretched zones at the outflow boundaries to eliminate disturbances with high streamwise wavenumbers before they reach the boundaries. The boundary layers are discretized with approximately 40 wall-normal points in both cases. The free-stream boundaries are streamline-shaped as can be seen in Figure 53; thereby, the free-stream disturbances introduced at the inflow boundary spread over the entire domain and leave it at the downstream outflow boundaries, optimally utilizing the discretized region. For the high-speed case, 5.28 million grid points are used, while 6.12 million grid points are used to discretize the low-speed case.

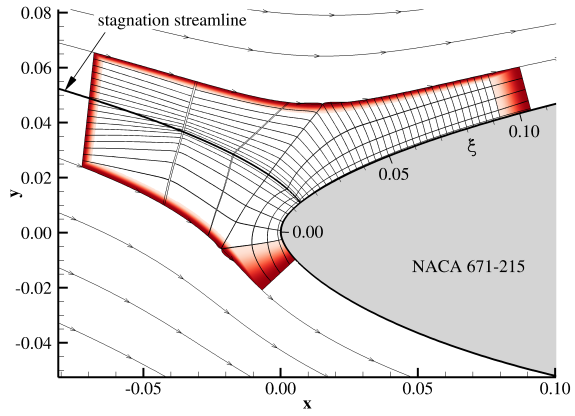

Figure 53: DNS domain used for the simulations of the high-speed case. The figure shows the domain decomposition, where each sub-domain has a resolution of 50 × 50 points. Sponge layers are placed in front of all boundaries but the wall.

For the investigation of receptivity to free-stream vortical disturbances, single wavenumber disturbances are introduced in the free stream. Starting in an arbitrary vortex system, streamwise invariant Fourier modes are used to define (incompressible) vortical disturbances. Streamwise vortical disturbances are introduced just downstream of the inflow boundary through volume forcing.

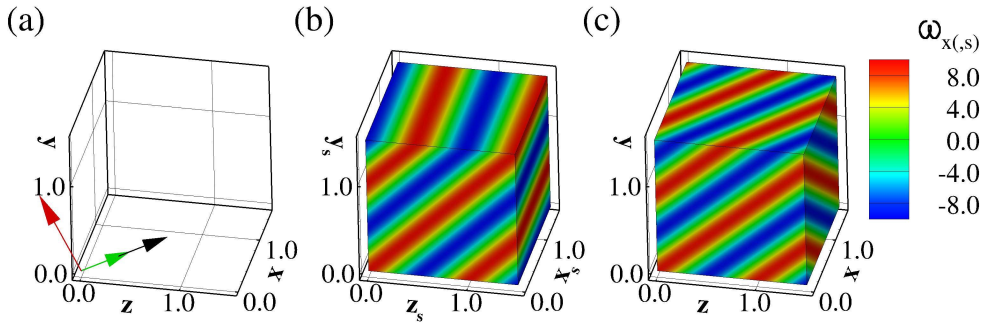

Figure 54: (a) Orientation of the free-stream velocity vector (black), the disturbance wave vector (red) and the disturbance vorticity vector (green); vector lengths are chosen arbitrarily. (b) Distribution of the streamwise vorticity $\omega_{x,s}$ in the streamline-oriented coordinate system. (c) Distribution of the vorticity ω_x in

A disturbance with amplitude $A = 10^{-3}$ and spanwise wavenumber of 786 is introduced in both cases. The downstream convection of the vortical disturbance for the low-speed case is shown in Figure 55. The contours indicate the vorticity components ω_x, ω_y, and ω_z. The distortion in the vicinity of the leading edge alters the orientation of the vorticity vector, leading to local amplitude changes in the single components. These vortical structures penetrate inside the boundary layer and trigger stationary

crossflow vortices. Figure 55 shows growth rates for steady crossflow modes based on LST. It is apparent that the latter is close to the LST value in the observed region.

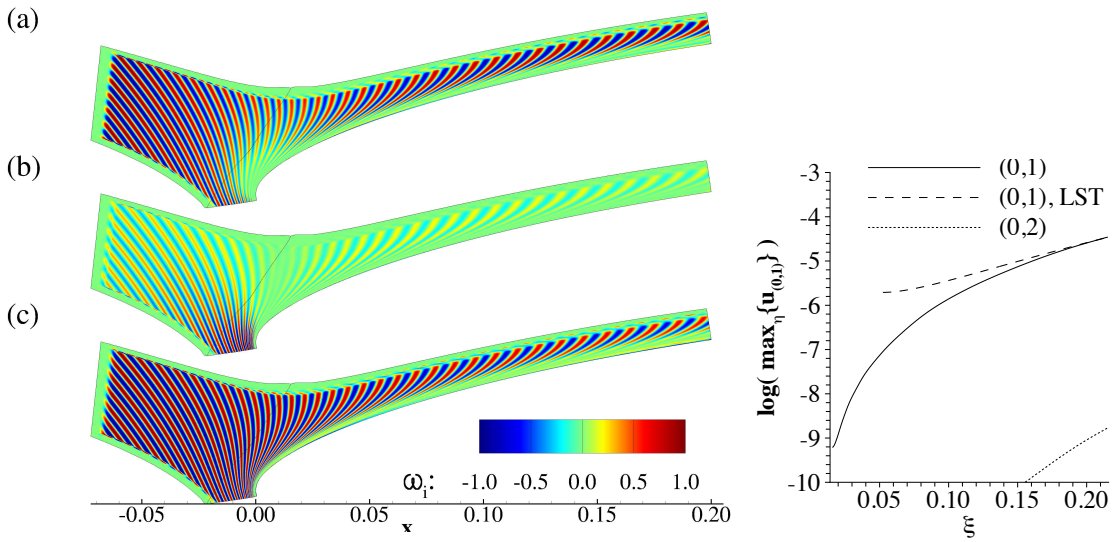

Figure 55: Right: Vortical disturbance with spanwise wavenumber 786 in the low-speed case, the stretched out- flow zones are not shown. The contours show the disturbance vorticity (a) ω_x, (b) ω_y, and (c) ω_z. Left: Downstream development of steady boundary-layer di turbance modes.

The investigation of the receptivity to steady vortical free-stream disturbances on a swept wing at low and high subsonic speeds shows that the receptivity is lower for the higher Reynolds-/Mach-number case. The disturbance wave vector was kept constant, and thus the considered mode is only near the growth maximum for the low-Re case. Typically, steady crossflow disturbances are excited by surface non-uniformities, but the study shows that they may be excited also by oncoming disturbances. The receptivity will not alter significantly if the frequency is non-zero but low, leading to even more amplified low-frequency travelling crossflow modes.

5.3.2 *Simulations of interaction of free-stream turbulence and roughness elements in an incompressible flow*

The simulations for studies of effects of freestream turbulence on the generation of crossflow disturbances excited by surface roughness have been performed by KTH and FOI for configurations corresponding to experiments by Hunt et al. and Downs et al. at Texas A&M University. In these experiments, distributed roughness elements are locally placed near the leading edge with a given span-wise wavenumber optimising the excitation of crossflow vortices. The response of boundary layer to both roughness elements and freestream turbulence is measured. Also the freestream perturbations are characterized to a great detail, reporting freestream turbulence length scales, intensity, spectrum, etc. This enables the numerical studies to reproduce the freestream perturbations in such analysis. The experiment used ASU(67)-0315 wing geometry designed to promote crossflow instability. These studies include variations of roughness height and their spanwise distribution as well as Reynolds number and freestream turbulence characteristics. In the experiment a wing model is mounted vertically in the wind tunnel. The incoming flow hits the leading edge at an angle of attack equal to α= -2.9°. The wing is mounted at a sweep angle of ϕ = 45° while keeping an infinite span condition. The negative angle of attack along with the design of the wing profile ASU(67)-0315 favors the growth of crossflow instabilities. The chord Reynolds number is $Re_C = Q_\infty C/\nu = 2.8\times10^6$ which is based on the long swept chord, i.e. $C = c/cos(\phi)$ = 1.83m, while c, the unswept short chord.

The main goal is to understand the effects on transition observed in experiments. Here, the isotropic homogenous freestream turbulence has been generated through DNS trying to match the characteristics of that measured in the experiments. The generated freestream fields are then applied as the inflow boundary condition for DNS of flow over the wing. A numbers of grids were generated to

check and chose an adequate resolution for simulations. The meanflow was computed using RANS solutions as boundary conditions.

The roughness elements were also placed at x/c = 0.029 similar to the experiment with a spacing L_z=12mm. The wavelength of the naturally most unstable stationary crossflow mode is λ_z=12mm. The height and diameter of the elements were chosen as ε_r =12μm and d_r = 3mm respectively. Three simulations are performed, one without the freestream turbulence, and two including the freestream turbulence with different turbulence length scales and intensities.

The freestream turbulence is reproduced to match the experimental data in terms of turbulence level and Taylor macro-scale. Both temporal- and spatial simulations have been performed to produce the turbulence filed (Figure 56). Two different cases has been studied. Tu=0.04% and 0.4%.

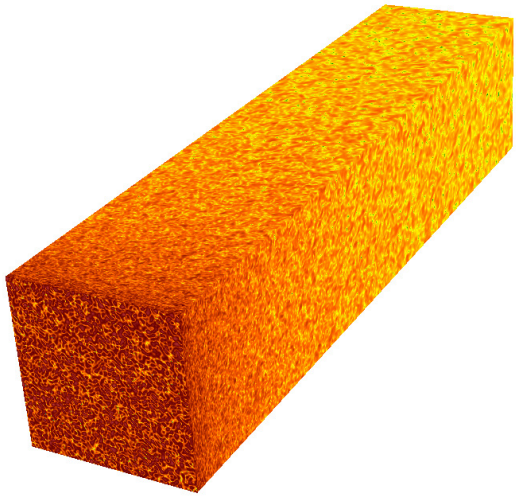

Figure 56: A sample of the box used in the generation of the freestream turbulence. At the inflow, randomly superposed Fourier modes are added on top of a constant velocity. The top and bottom along with the lateral side have periodic boundary conditions. Isosurfaces of perturbation energy, drawn at ±0.0001|v′|.

Different methods have long existed for generating freestream isotropic turbulence. A very low level of freestream turbulence as is reported in the experiment, results in a very low Taylor's micro-scale Reynolds number. In order to generate the freestream turbulence at this low level, randomly superposed Fourier modes are fed into a box which has periodic boundary conditions on the lateral sides and at the top and bottom. An inflow condition has been used and the width of the rectangular box is chosen to correspond to the spanwise length in the three-dimensional wing simulation. In our study that length corresponds to 12mm, which is the most unstable stationary mode. The flow cases studied are given in Table 3.

Case Name	Roughness height h	Turbulent intensity Tu	Integral length scale L	Re_λ
Tu04–12	$12\mu m$	0.04%	12mm	2
Tu04–36	$36\mu m$	0.04%	12mm	2
Tu40–00	$0\mu m$	0.40%	12mm	20
Tu40–36	$12\mu m$	0.40%	12mm	20
Tu40–36	$36\mu m$	0.40%	12mm	20

Table 3: Selected cases with different turbulent characteristics and roughness heights.

Each simulation approximately consumes 1 million core hours. Figure 57 shows a comparison with respect to transition location between the five cases. Instantaneous spans-wise velocity components are shown, and the iso-surfaces are colored with the value of the local streamwise velocity. The transition location changes in time for all the cases. It is exacerbated for the case without the roughness element (Tu40–00). The transition is dominated by the non-stationary crossflow vortices. Once the roughness is introduced, the transition shifts significantly upstream. There is roughly a 20% shift in transition location comparing the case Tu40–00 with Tu40–12 and Tu40–36 where the turbulent intensity level is 0.4%. The transition location comparison between Tu40–12 & Tu40–36

from or Tu04–12 & Tu04–36 could be inconclusive base on the instantaneous snapshots, therefore a time-averaged friction coeffcient could prove to be more conclusive.

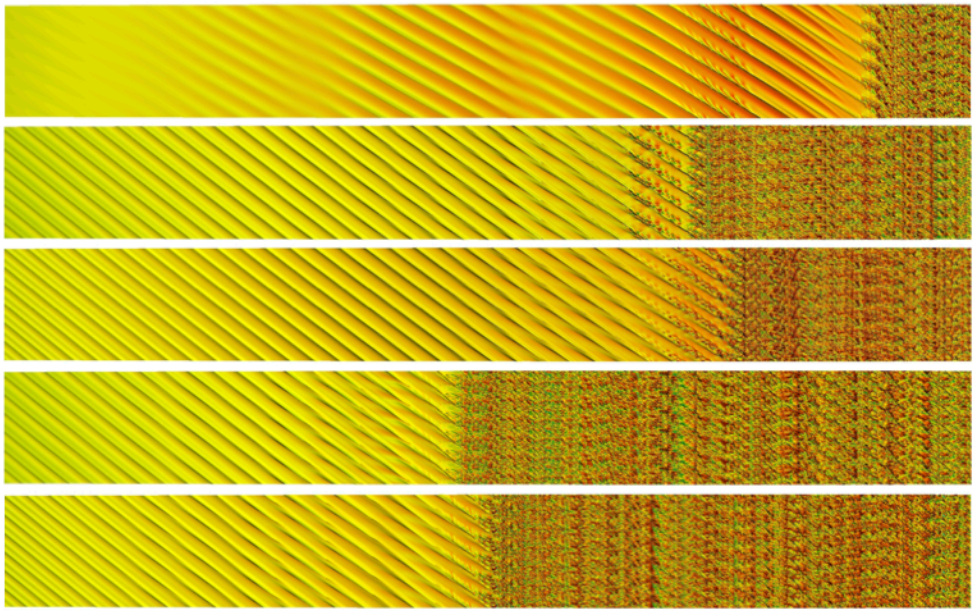

Figure 57: Isosurfaces of spanwise velocity components colored with the magnitude of the streamwise velocity component. From the top, case: Tu40–00, Tu04–12, Tu04–36, Tu40–12, and Tu40–34. Five spanwise periodic domains are shown for visualization purposes. The crossflow vortices could be visibly seen, and emergence of turbulent spots and the final breakdown to turbulence.

It could be seen that the transition location shifts upstream as the level of freestream turbulence is increased by one order. Note that these values of freestream turbulence are reportedly at a very low range. The transition location shift could be better shown by looking at the time averaged friction coefficient in Figure 58a. A 10% shift in transition location is visible. In Figure 58b, the transition location from DNS is compared with those observed in the experiments. The roughness element has the same characteristics as in the experiment. It could be seen that there is a shift in transition location for similar turbulence intensities between experiment and simulations. The trend however seems to be consistent with the experiment and an increase in the turbulent intensity shows the same linear behavior.

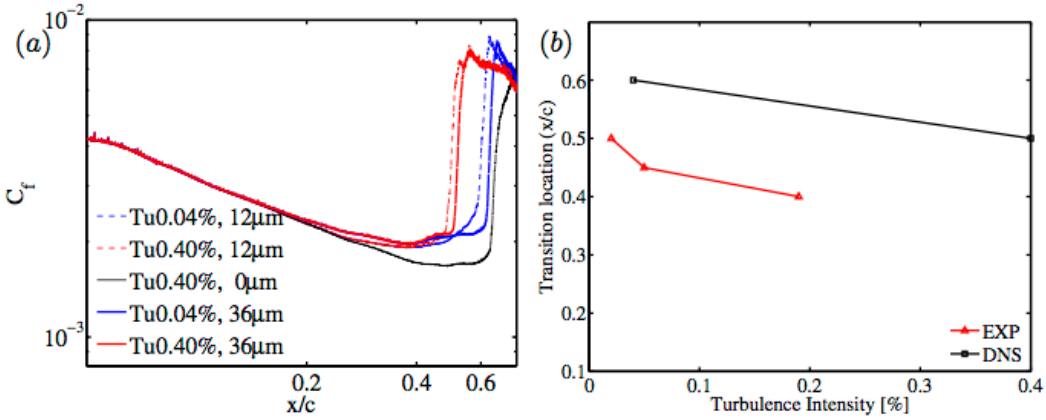

Figure 58: a) Time-averaged friction coefficient for cases with different turbulence intensities and roughness heights. (b) Transition location as a function of turbulence intensity for roughness height of 12 micron.

It appears that the receptivity to freestream turbulence in the presence of roughness elements has a linear behavior in that regime and it is dominant near the roughness location. No additional receptivity mechanism could be detected along the streamwise direction away from the roughness. It was

observed that the presence of merely freestream turbulence gave rise to the emergence of weak travelling crossflow vortices. These vortices however also breakdown near the trailing edge, and the transition location appears to fluctuate more as compared to the cases where an array of roughness element is present.

Increasing the roughness height (in the range studied here) proved to have a stabilising effect, when two cases with the same turbulence intensities were compared. This could be explained in the dominance of the stationary crossflow modes, and a more bulbous meanflow profile when the roughness height is increased. All the cases were performed for a critically spaced array of roughness element. Critically, refers to the spanwise spacing which excited the most unstable crossflow mode.

6 Receptivity analysis

6.1 Validation of receptivity-prediction tools

Two different cases where chosen for comparison of methods used by different partners. The first one corresponds to the direct numerical simulations performed by Schrader et al. (JFM 2009). The boundary layer is of Falkner-Skan-Cooke type with a Hartree parameter of $\beta_H=0.333$. The second case corresponds to the experiments by Reibert, Saric & co-workers at Arizona State University (Reibert et al. 1996 AIAA paper 96-0184). Mean flow has been performed by FOI and distributed to other partners using EUROTRANS format.

FOI/KTH used their receptivity code based on the adjoint of PSE to compute the receptivity to surface roughness. The results corresponding to Schrader et al. is given in Figure 59. As seen there, an excellent agreement with the DNS data is found.

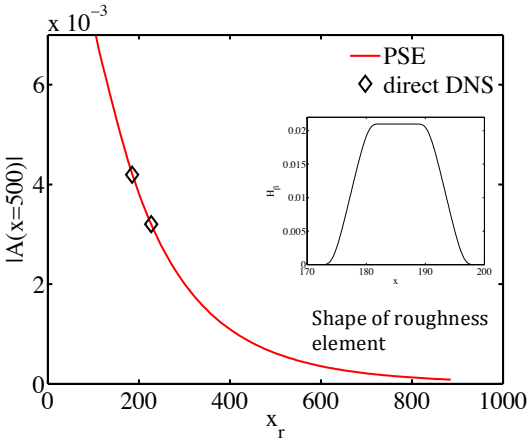

Figure 59: Equivalent amplitude of a crossflow mode measured at $x=500\delta^*$ as a function of roughness location.

The results for experiment by Reibert et al. are shown in Figure 60. As can be seen here not only the fundamental mode amplitude is predicted correctly, but also estimation of higher harmonics amplitudes are good.

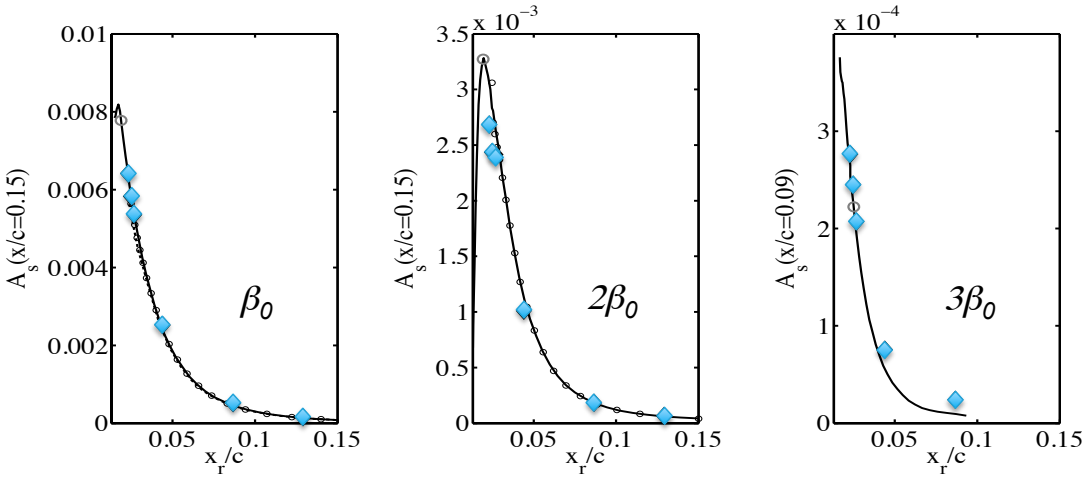

Figure 60: Amplitude of generated cross-flow perturbations at location of roughness elements. NLF (2)-0415 airfoil at 45º sweep.

Further, CIRA has extended the compressible 2D receptivity method based on multiple scale approach to 3D. The code has been validated by comparing the receptivity amplitude for a defined test case. As is shown in Figure 61, the obtained results based on the multiple scale is in perfect agreement with those computed by FOI/KTH using an approach based on the adjoint PSE. This shows that both methods include the effects of nonparallel flow at the same degree.

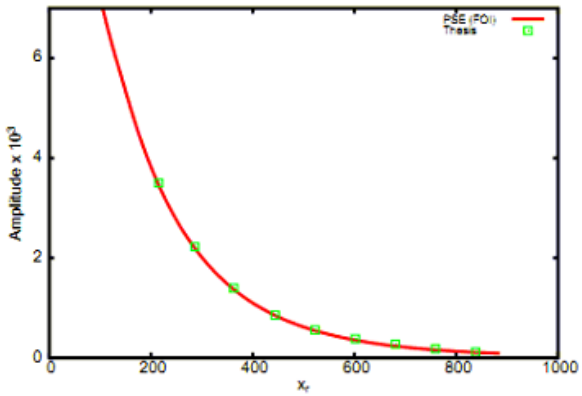

Figure 61: Receptivity amplitude computed by CIRA-UNISA using a multiple-scales method (symbols) compred to FOI/KTH results based on the adjoint PSE (solid line).

Validation of the DLR receptivity tools for discrete surface roughness based on Finite Reynolds Number Theory (FRNT) has been started by considering the Reibert et al. (AIAA 1996) test case and the Schrader et al. (JFM 2009) test case. For the Reibert et al. test case receptivity analyses for the given roughness geometry, linear and nonlinear nonlocal instability computations have been performed so far. For the Schrader et al. test base linear local and nonlocal stability analyses followed by receptivity studies have been performed (Figure 62). In both cases the laminar basic flow data sets provided by KTH were used.

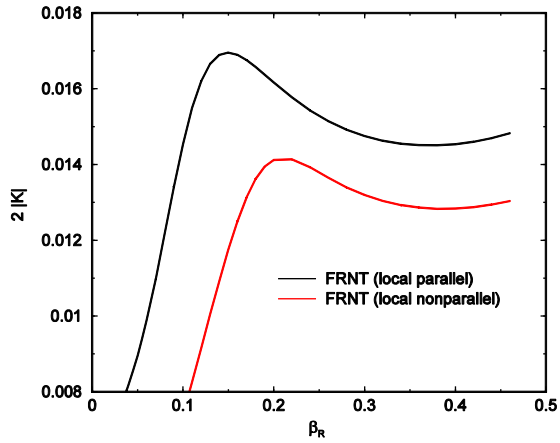

Figure 62: Receptivity coefficient for roughness at x=186.2 as a function of spanwise wavenumber β for the Schrader et al. test case.

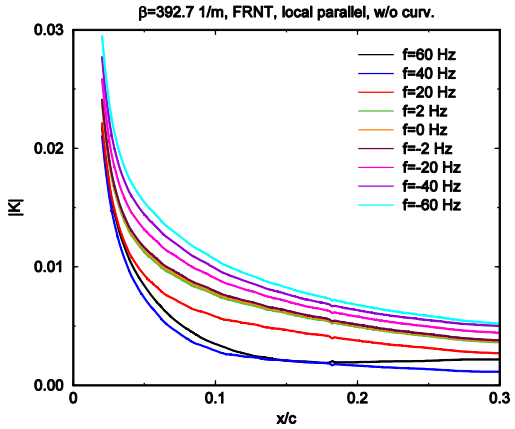

Figure 63: Receptivity coefficients computed for conditions of experiment A.

6.2 Effects of roughness shape on the receptivity coefficient

Linearized boundary conditions are a commonplace numerical tool in any flow problems where the solid wall is nominally flat but the effects of small waviness or roughness are being investigated. Typical are stability problems in the presence of undulated walls or interfaces, and receptivity problems in aerodynamic transition prediction or turbulent flow control. One UNISA contribution to the computation of receptivity to wall roughness has consisted in the clarification of when and to what extent the disturbances produced by the wall can be considered to depend linearly on the height of the wall roughness.

To properly pose such problems, solutions in two distinguished mathematical limits have to be considered: a shallow-roughness limit, where not only roughness height but also its aspect ratio becomes smaller and smaller, and a small-roughness limit, where the size of roughness tends to zero but its aspect ratio need not.

Here a connection between the two solutions is established through an analysis of their far-field behaviour. As a result, the effect of the surface in the small-roughness limit, obtained from a numerical solution of the Stokes problem, can be recast as an equivalent shallow-roughness linearized boundary condition corrected by a suitable protrusion coefficient (related to the protrusion height used years ago in the study of riblets) and a proximity coefficient, accounting for the interference between multiple protrusions in a periodic array.

A "protrusion coefficient" was introduced as necessary corrections for the situation where the linear regime is exceeded. This study was extended further by introducing a proximity coefficient to account

for the interaction of multiple roughness elements arranged in a periodic pattern. Examples of both the protrusion coefficient and proximity coefficient are given in Figure 64. These corrections have been published in P. Luchini: "Linearized no-slip boundary conditions at a rough surface", *Journal of Fluid Mechanics 737, 349-367 (2013)*. From an application viewpoint these results imply that the classical linearized boundary condition employed in either already developed or to-be-developed simulation codes can a) be trusted as is if the aspect ratio of protuberances (or cavities) is within the acceptable range (for instance ± 0.02 for an error of 10%, or b) corrected through a protrusion coefficient, if the aspect ratio is larger but irregularities are sparse, or c) further multiplied by the proximity coefficient, if interaction between irregularities becomes important.

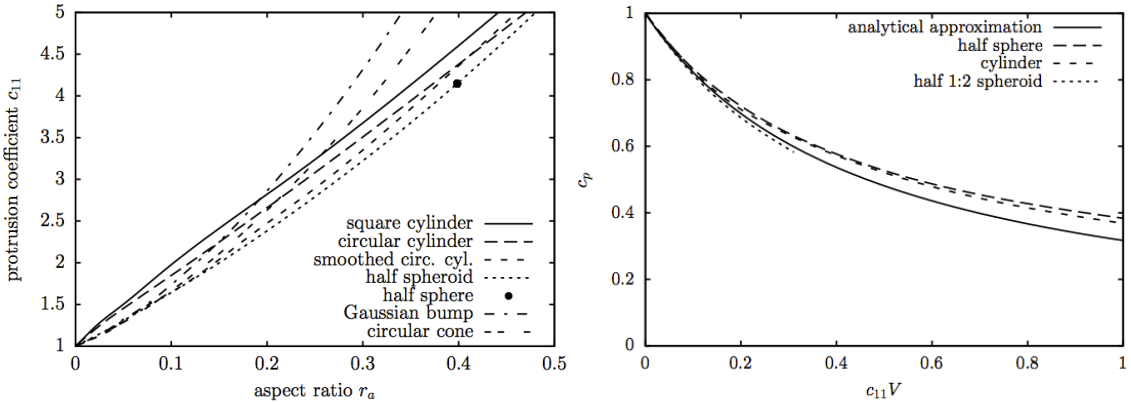

Figure 64: Left: Protursion coefficient. Right: Proximity coefficient.

6.3 Receptivity to thermal noise

A general difficulty encountered in applying quantitative receptivity calculations to transition prediction is the quantification of external disturbance sources. Of these the easiest to be characterized quantitatively is surface roughness, although even for this quantity measurements are not always available. External sources of acoustic noise and turbulent fluctuations are, on the other hand, generally unknown, especially under free-flight conditions. By this we mean that little or no data is available about the natural sources of such noise. Different is, of course, the case of wind-tunnel experiments where noise is artificially introduced, which constitute an important contribution elsewhere in this project.

One source of disturbances that received only occasional attention until today is thermal noise arising from microscopic molecular agitation. Yet thermal noise is present in fluids just like in any other physical system, and in the presence of amplification phenomena (receptivity) it can produce macroscopic consequences. In addition, thermal noise is quantitatively well known, and constitutes the minimum amount of noise that can be present in any system without violating the laws of thermodynamics. One UNISA contribution to the RECEPT project has been the inclusion of thermal noise in receptivity computations.

The fluctuation-dissipation theorem, a well-established landmark of statistical mechanics, stipulates that every macroscopic dissipation phenomenon is accompanied by a random forcing, representing the thermal fluctuations induced by the underlying microscopic mechanics. Manifestations of this principle are, for instance, Brownian motion in a suspension and the input noise of an electronic amplifier. The concept is particularly well developed in electronics, where internal noise limits the sensitivity of any detector device (for instance, a radio receiver or an instrumentation amplifier) and the best amplifiers are not far from the minimum noise level provided by thermal noise. In fact, the noise figure commonly quoted among the commercial specifications of an amplifier is nothing else than the ratio of the actual noise level to theoretical thermal noise. And, once a noise figure of 1 (or 0 dB) is approached, nothing can be done to further improve the signal-to-noise ratio other than physically cooling the device to low temperature, a measure actually taken in some cases (infrared cameras are an example). The fluctuation-dissipation theorem sets a lower bound to the thermal noise

present in any amplifier, electronic or otherwise, below which the second law of thermodynamics would be overthrown.

Figure 65 presents the main result of these investigations, and show for each test case the r.m.s. thermal-noise-induced velocity fluctuation amplitude as a function of Re_x and, respectively, N-factor. It can be observed that for all the tested profiles the N-factor where a noise amplitude of 0.01 is attained is significant lower than for Blasius, and in the general neighbourhood of N=10. All these results lead us to believe that receptivity to thermal noise is an important instrument in transition prediction, which eliminates the uncertainty about external noise sources and provides an upper bound on the transition threshold which is actually not far from where transition is observed in experiments. Actually, it could be proposed that in future receptivity analyses other noise sources be characterized by a ”noise figure”, just as routinely adopted in electronics, that is by the ratio of their effects to the effects of thermal noise. The benefit of such a concept could possibly be a generalized collapse of data and eventually the capability to overcome the general unavailability of data about noise sources that induced a change in some objectives of the present project.

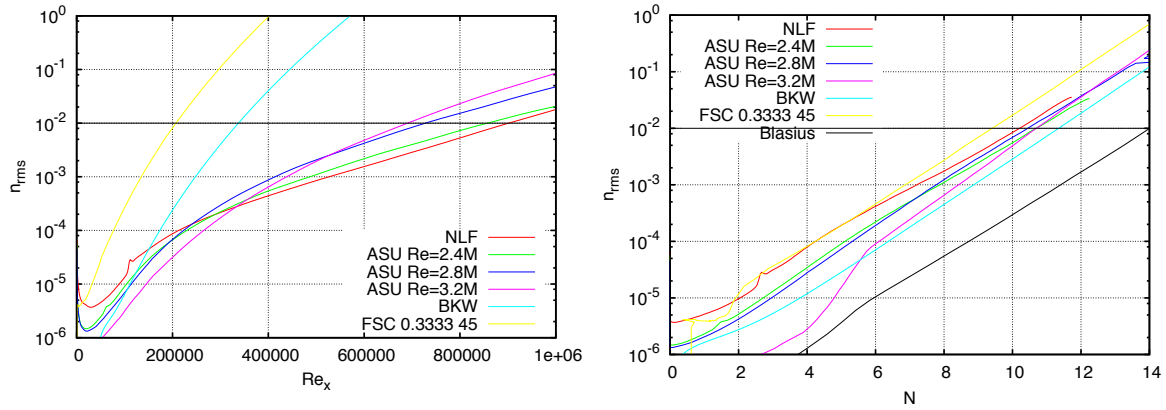

Figure 65: r.m.s. of thermal-noise-induced velocity fluctuations (n_{rms}) as a function of local Reynolds number and N-factor for selected cases.

6.4 Application of receptivity tools to RECEPT data

The pressure distribution from the CFD computations by FOI was used to perform the boundary-layer computations. CFD computations were performed in design-stage of the experiment A. In these computations the wind tunnel walls were included and their shape corresponded to the one used in the experiment. As can be seen in Figure 66, the downstream development of the computed edge-velocity is slightly from the measured one. The experimental data show a weaker pressure gradient compered to the calculated data. This can give a different growth rate of crossflow vortices. To examine that, the computed boundary-layer flow based on the scaled CFD data was used to perform stability analysis. As can be seen in Figure 66 the agreement was not satisfactory.

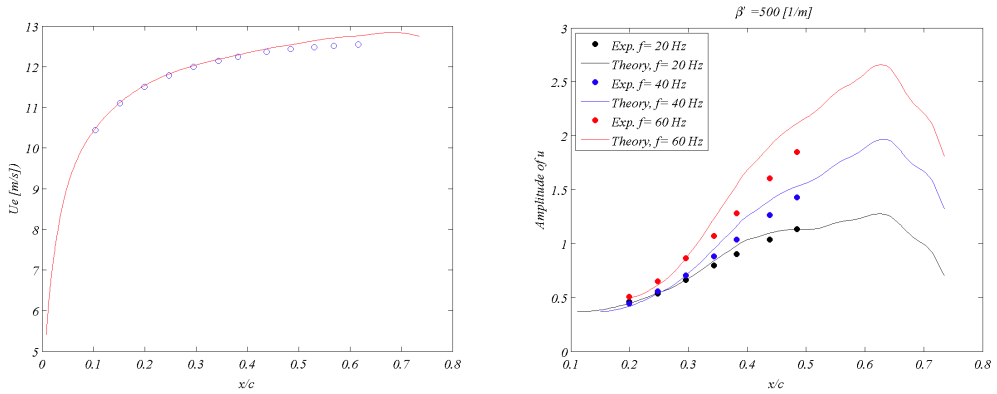

Figure 66: Comparison of measured and computed values of the streamwise velocity component (left) amplitude of crossflow modes (right). The amplitudes are scaled to match the experimental ones at x/c=30%.

In order to improve the agreement between the measured and computed disturbance amplitude, different approach to modify the pressure distribution were tried. First the pressure distribution in the downstream portion of the airfoil was changed such that the obtained velocity distribution matched the measured one. Then, the pressure distribution close to leading edge as well as location of stagnation point was modified until close agreement between the measured and computed disturbance amplitudes were reached. The variation of stagnation point was around 1% of the chord. This was made to mimic the possible effect of the traversing system on the velocity field around the model. In Figure 67 values of the edge velocity from computations and measurements are plotted. Here, also the amplitudes of crossflow modes with frequencies f=40 Hz and different spanwise wavenumbers are plotted. As can be observed there, the new pressure distribution gives a close agreement between the computed and measured data.

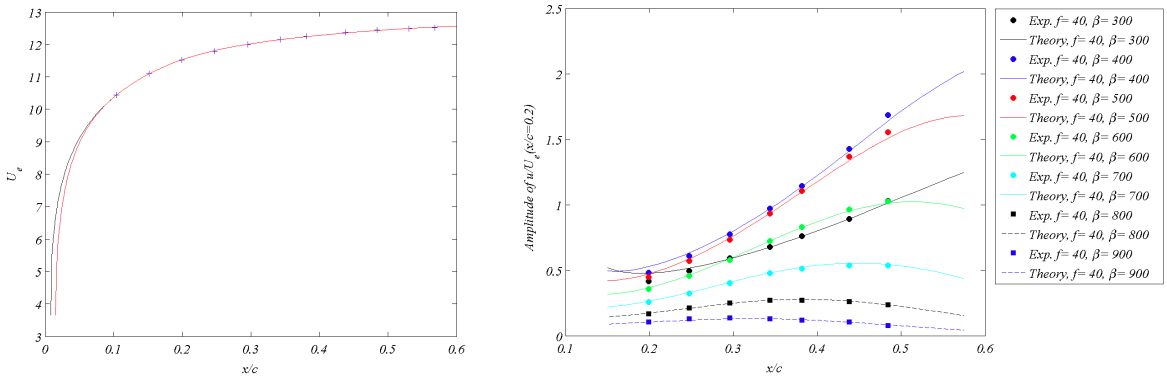

Figure 67: Comparison of measured and computed values of the streamwise velocity component (left) amplitude of crossflow modes (right) based on the modified pressure distribution. The amplitudes are scaled to match the experimental ones at x/c=34%.

Similar analysis was performed for data of Experiment B. Further, the receptivity of the vibrating elements studied in Exp. A was investigated. The receptivity coefficients for unsteady crossflow vortices (waves) were computed using an adjoint-based method. The results based on the local and nonlocal/PSE computations are presented in Figure 68. A difference between the estimated and measured coefficients is observed, which can be due to different scaling of data.

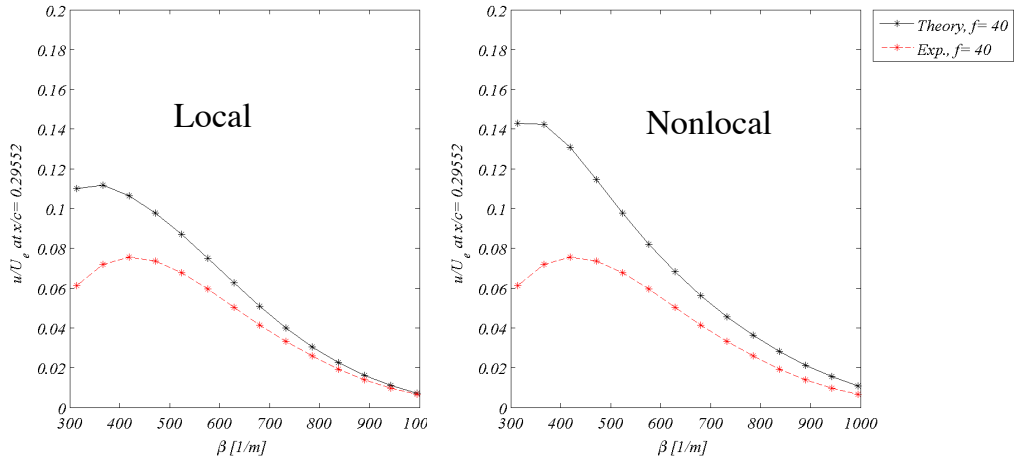

Figure 68: Comparison of receptivity coefficients for an unsteady crossflow mode with frequency of 40 Hz.

The receptivity of the compressible three-dimensional boundary-layer flow over the RECPT wing geometry was studied. This corresponds to the flow case studied by STUTT in WP2. The flow filed was extracted from DNS and written in EUROTRANS format for stability and receptivity analysis. Some smoothing of data was made to remove small oscillation in the derivatives of velocity profiles. In Figure 69 (left) the amplitude evaluation of the generated crossflow vortices from DNS is compared

to that given by the linear nonlocal/PSE stability analysis. As can be seen there, an excellent agreement is found which shows that the perturbation amplitude is in linear range.

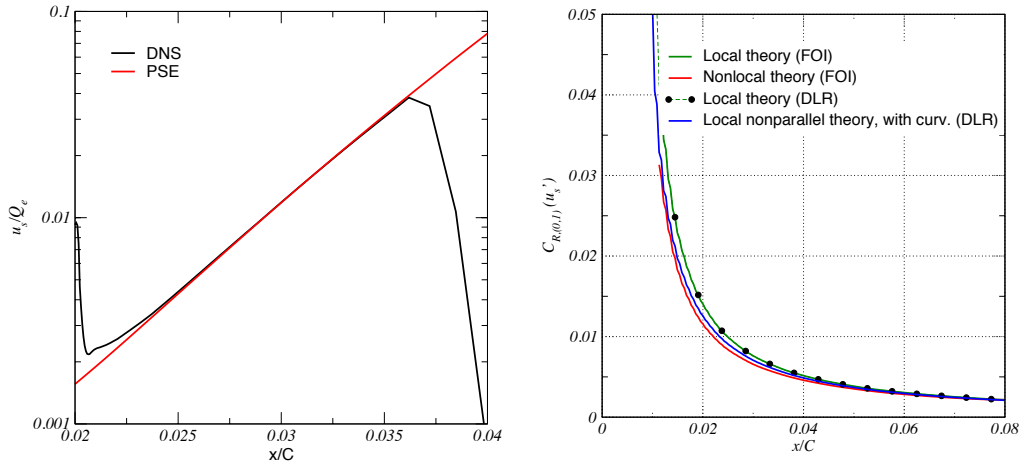

Figure 69: Amplitude of the cross flow vortices (left). Comparison of receptivity coefficient computed by different methods.

The receptivity coefficient was computed either using an adjoint-based approach (FOI) or a residual-based method (DLR). As can be observed in Figure 69 (right) the agreement between the results form different approaches is very good. Further, the amplitude of the crossflow generated by these roughness elements was estimated using the receptivity coefficient and actual shape of the roughness elements. For this purpose, the Fourier transform of the roughness shape was computed. Including the protrusion coefficient developed and computed by UNISA the difference between the estimated amplitudes and those found in DNS was less than 1%. The amplitude of perturbations was also computed by assuming the roughness elements having exact cylindrical shapes. In that case the Fourier transform of the roughness elements can be computed analytically. These results were also close to DNS data.

7 New approaches for nonlinear transition prediction

7.1 Transition prediction based on characteristics of stationary cross-flow vortices

The field of secondary stability is concerned with the study of the linear stability of steady or quasi-steady flow states resulting from the growth of previous instabilities (termed primary instabilities) to finite amplitudes. In achieving finite amplitude, the primary instability may saturate thereby attaining a new steady state which in turn modifies the original flow under consideration. It is this new flow whose linear stability is of interest, motivated by experimental observations in which secondary instabilities arise shortly before transition to turbulence occurs.

The idea behind the present studies has been two-folded:

- Application of secondary N-factor (N-factor based on the secondary instability) for selected cases.
- Correlation of characteristics of modified stationary flow with transition location.

To conduct these analyses, KTH together with FOI has developed a code for computations of secondary instability of the stationary cross-flow vortices. The discretization is optionally based on Chebychev polynomials or high-order finite differences. The mean flow is either taken in the physical- or in the Fourier space. The code was further developed by UNIGE to perform the N-factor computation of the secondary instability. The code has been validated by comparison with results from the ALTTA project.

To make the code robust and fast for computations of secondary N-factor, the Inverse Iteration Algorithm (IIA) for both temporal and spatial stability analysis was implemented. The approach is based on an iterative method. This gives the possibility to track a single secondary instability mode along the streamwise direction, which is required for computation of secondary N-factors. The implementation of spatial secondary-instability gives the possibility to skip the Gaster transformation, which can introduce non-negligible differences from the exact values of spatial growth.

The tool has been applied to a number of test cases to analyse the secondary instability of the stationary crossflow vortices. The procedure has been as follows.

1. Nonlinear PSE calculations of stationary crossflow vortices were performed with initial amplitude of perturbations given by receptivity computations.
2. A global solution was computed downstream, within the experimentally found transition region, for each base flow.
3. The unstable modes computed in step 2 were used as initial guess for the IIA at the most downstream position; with a converged solution the IIA was then applied at the next discrete upstream position. This was continued until the most upstream position was reached.

The ASU flow case were chosen for application of secondary N-factor and our new approach. A series of 2.5D RANS simulation for the wing model installed in the windtunnel (Hunt & Saric's experiments) has been performed to compare the computed pressure distribution with the measured ones. A good agreement was achieved between the CFD results and measured pressure coefficients (see Figure 70). The meanflow computations for different test cases were performed and the distributed to partners in EUROTRANS format.

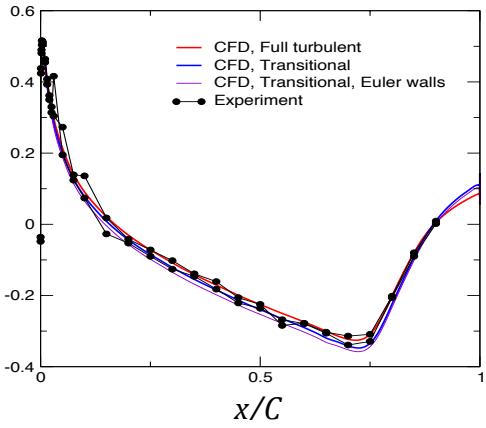

Figure 70: Comparison of measured and computed pressure distribution of Hunt & Saric experiments.

Linear stability analysis for Hunt & Saric's experiments (ASU geometry) at three different Reynolds numbers gave a transition N-factor of approximately 8 for stationary CF and 12 for traveling CF waves (for all cases). The results are shown in Figure 71.

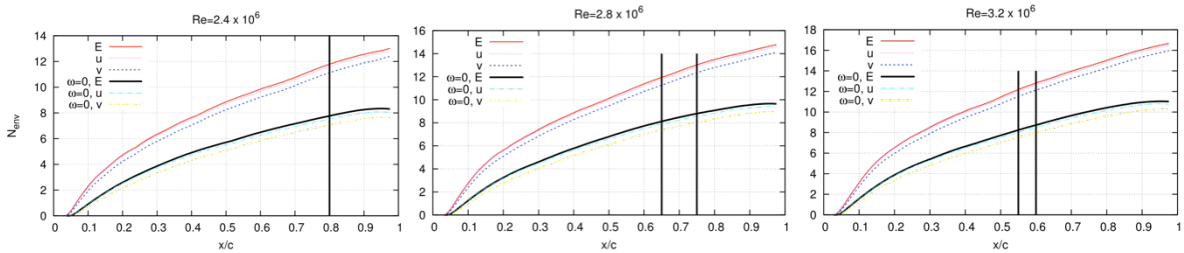

Figure 71: Envelope of nonlocal N-factors for Hunt & Saric's experiments. Vertical lines indicate transition location.

Receptivity analyses have also been performed for these cases to find an approximation for initial amplitude of the stationary CF vortices. These amplitudes have been used in nonlinear PSE computations. In Figure 72 results of typical simulations are shown. The goal of these studies is to find a correlation between the amplitude of stationary CF vortices and transition location.

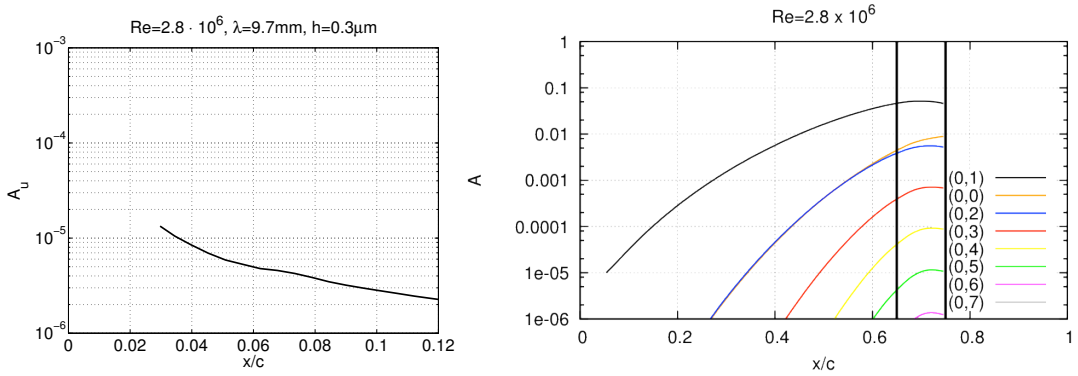

Figure 72: Initial amplitude of stationary CF vortices as a function of x/c computed by adjoint methods (left) and nonlinear PSE computations (right).

The meanflows modified by stationary crossflow vortices were used for secondary instability analysis. Figure 73 gives an example of secondary N-factor computations for one of ASU cases.

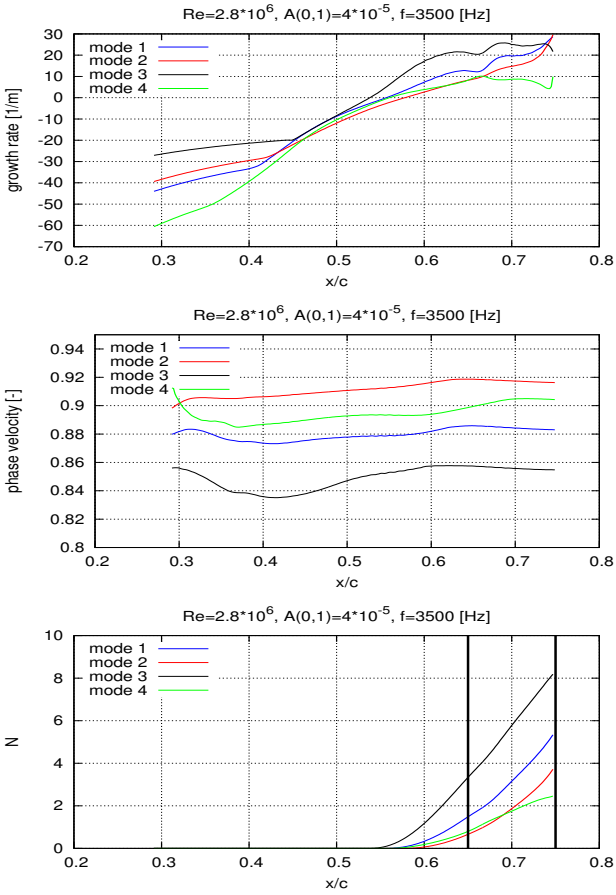

Figure 73: (top) Spatial growth rate, (middle) phase velocity, (bottom) amplification, all as a function of the streamwise coordinate for four different modes, all with f = 3500 Hz. Re=2800000, A(0,1)=4×10$^{50-5}$ and β_{n50} =10.

It is known that transition in crossflow-dominated flows is caused by by breakdown of these vortices. This breakdown is a consequence of their secondary instability. Therefore, it was suggested to investigate the onset of the secondary instability for the ASU experiments and try to find a correlation between that and the transition location. In Figure 74 the ratio of chord position of the neutral point and the upstream measured transition location is presented as a function of the initial amplitude of the fundamental mode for the different Reynolds numbers. A similarity is found, at least for Re = 2800000 and Re = 3200000. Since the transition location in the case of Re = 2400000 was not measured but assumed to occur where the separation point is measured it is clear that the data is less reliable. However, if we assume an ”extrapolated” transition location (0.85 instead of 0.8) the similarity holds also in this case. This might indicate that it is possible to estimate the upstream neutral position of the secondary instability, which is in the vicinity of the transition location, if the initial amplitude of the primary disturbance is known.

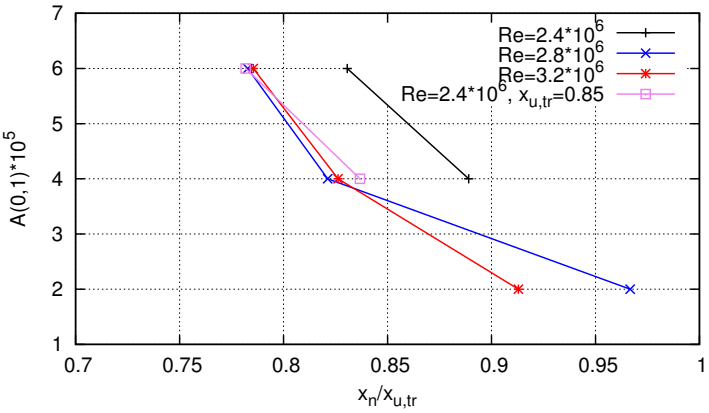

Figure 74: Ratio between the upstream neutral position and the upstream measured transition position, for two different Reynolds numbers.

These studies were taken on step further and the relation between the onset of secondary instability with the characteristics of the modified meanflow was investigated. Different criteria for the onset of secondary instabilities can be found in the literature. In the investigation by Bottaro & Klingmann (1996), regarding the nonlinear evolution of Görtler vortices in the flat plate boundary layer, they showed that a properly scaled value of the spanwise shear is constant in the streamwise direction. A similar idea is developed here where we investigate if there exist a dimensionless parameter, here denoted Re_n, with a ”universal” value at the location of the upstream neutral position of the secondary instability. The motivation comes from the notion that, in many cases, the experimentally measured transition location is found just downstream of neutral position. In those cases the secondary instability onset is already a clear indication that transition will occur shortly after. With a universal value Re_n it would therefore be possible to detect the location of the transition onset without actually having to perform the secondary instability analysis. It is known that the secondary instability is related to the inflection points in the wall-normal and spanwise directions. In this work, the correlation between two new Reynolds numbers ($Re_{n,y}$, $Re_{n,z}$)based on the normal and spanwise shear scaled with local displacement thickness and edge velocity with secondary instability is investigated. Results for ASU test cases are found in Figure 75, where the onset of spatial secondary instability is marked with an open circle. We can see that both values are approximately constant, at the location of the instability onset, comparing the different base flows with $Re_{n,y} \approx 400$ and $Re_{n,z} \approx 50$.

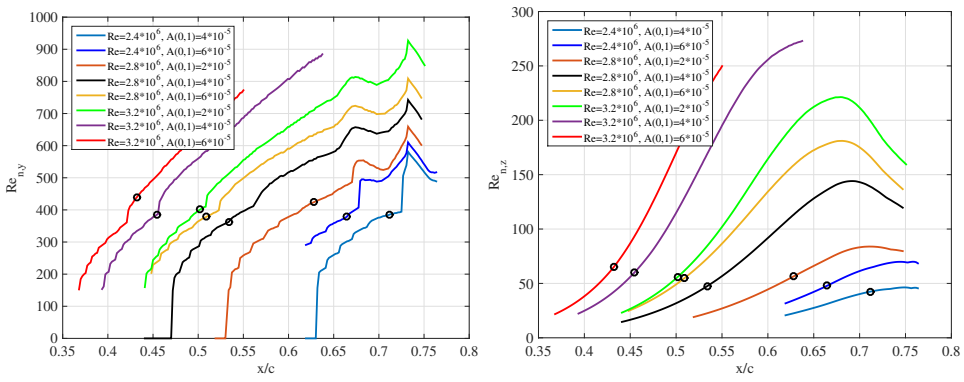

Figure 75: Onset Reynolds number $Re_{n,y}$ (left) and $Re_{n,z}$ (right) as a function of x/c. The open circles show the locations of the upstream neutral points of the secondary instability.

This method has also been applied to two cases published in Downs’ thesis, which have also been studied through DNS by KTH in WP2. The values for one of cases were $Re_{n,y} \approx 350$ and $Re_{n,z} \approx 50$m while another one gave values 210 and 40, respectively (see Figure 76).

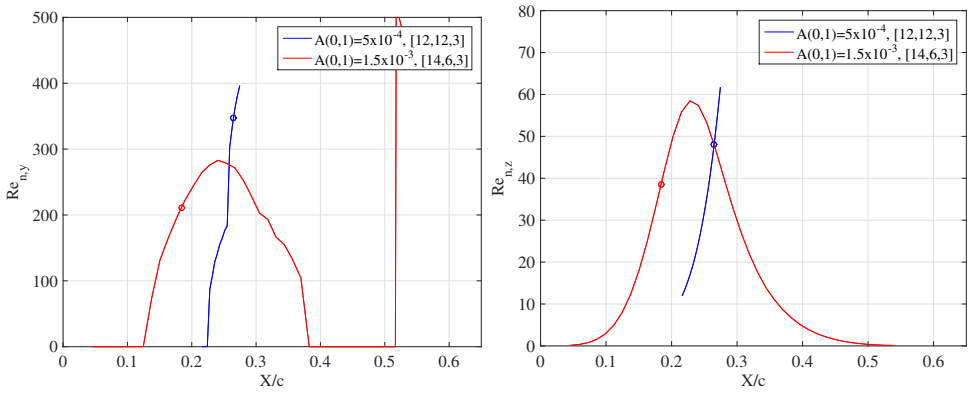

Figure 76: Onset Reynolds number $Re_{n,y}$ (left) and $Re_{n,z}$ (right) as a function of X/c for the cases [12,12,3] and [14,6,3] and two different values of A(0, 1). The circles indicate the corresponding upstream neutral points of the secondary instabilities.

7.2 Coupling of secondary-instability analysis and nonlinear PSE

Besides the amplitude-based transition prediction concept for crossflow-dominated transition scenarios described above another alternative approach has been developed in RECEPT. As in the first approach nonlinear PSE is used to model the nonlinear saturation of primary crossflow vortices. However, in this alternative approach the growth of secondary instabilities is directly modeled within nonlinear PSE and secondary instability theory is only used to provide suitable initial conditions for secondary instabilities within nonlinear PSE. More precisely, the PSE computations provide the input data for the secondary instability code and its results in turn are used for initialization of the secondary instabilities within the PSE analysis. According to our knowledge, it is the first time that such an approach with bi-directional coupling of both numerical methods has been used for amplitude-based transition prediction. The advantage of this approach is that it covers both the linear and nonlinear stages of secondary instability growth including an additional rise in skin friction and the nonlinear feedback of the secondary disturbances on the 'primary' crossflow vortices. Thus, a secondary N-factor method for predicting the transition location is no longer needed. Moreover, it is much more efficient than modelling the high-frequency secondary instabilities as higher harmonics of travelling crossflow vortices, because much less Fourier modes are needed in the new approach.

The ALTTA project was the first EU project where results from nonlinear PSE were used as input for subsequent secondary instability analyses. The first test case chosen in ALTTA had been the DLR swept flat plate experiment of Bippes and co-workers. Therefore, this configuration has been chosen also within RECEPT for testing the newly proposed approach. For the example shown here, stationary crossflow vortices of fundamental spanwise wavelength are initialized at a chord position $x_c/c\approx0.04$, represented by Fourier mode (0,1) in the nonlinear PSE computations. Slightly further downstream the stationary crossflow vortex mode starts to be amplified and as its amplitude increases successively higher harmonics (0,n) are nonlinearly generated (Figure 77 left). Due to these modes regions of high shear develop in the mean flow which support the development of high-frequency secondary instabilities. Therefore, at $x_c/c\approx0.70$ the resulting mean flow is extracted and used as input for a secondary instability analysis. The frequency of about 2640 Hz chosen for the secondary mode is about twenty times higher than those of the most amplified travelling crossflow waves and according to secondary theory this mode is almost neutrally stable at this downstream position.

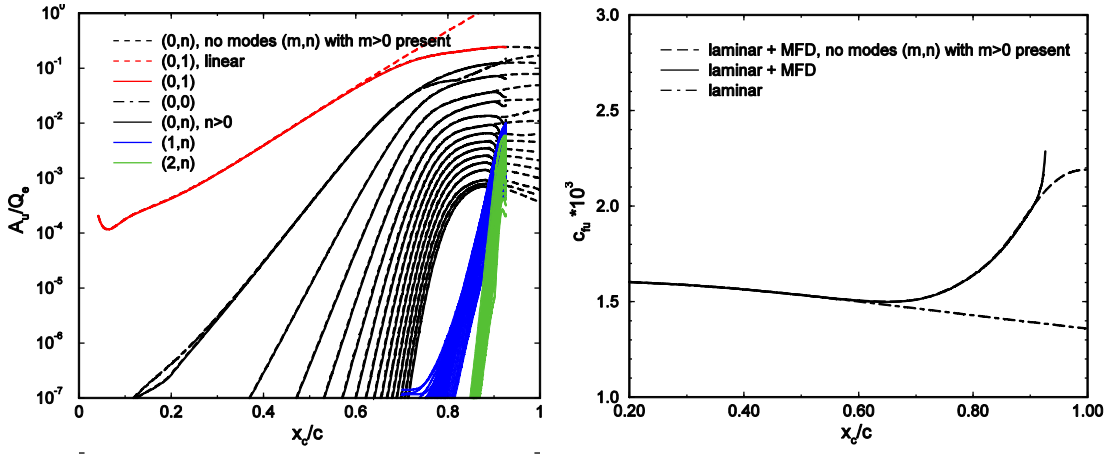

Figure 77: Left: Nondimensional chordwise velocity amplitude of different Fourier modes (m,n) with m denoting the m-th harmonic of the fundamental frequency f_0≈2640 Hz and n denoting the n-th harmonic of the fundamental spanwise wavenumber $\beta_0 \approx 523.6\ m^{-1}$. Dashed black lines: PSE results on the development of the stationary crossflow vortex and its higher harmonics, (0,n), $1 \le n \le +16$, and the mean flow distortion (MFD) mode (0,0) without presence of any unsteady disturbance. Coloured solid lines: Corresponding PSE results for a case where an additional secondary instability mode was initialized at chord position x_c/c= 0.70. In red: stationary crossflow vortex, its higher harmonics and the MFD. In blue: the secondary instability mode represented in the PSE computations by the Fourier modes (1,n), $-16 \le n \le +16$. In green: the nonlinearly generated first temporal higher harmonics (2,n), $-16 \le n \le +16$. Right: Corresponding chordwise skin-friction coefficient of the resulting spanwise-averaged mean flow for the cases with (solid) and without (dashed) secondary instability mode initialized and compared to the laminar value (dash-dotted).

Figure 78 shows the resulting temporal secondary eigenspectrum with the isolated marginally stable secondary eigenvalue and the corresponding two-dimensional eigenmode structure used to initialize the secondary instability at $x_c/c \approx 0.70$ in the PSE computation. Within the PSE approach the structure of the single secondary eigenmode is represented by a packet of Fourier modes (m,n) with m=1 and $-16 \le n \le +16$, where the first index m and second index n denote the m-th harmonic of the fundamental frequency f_0 and the n-th harmonic of the fundamental spanwise fundamental wavenumber β_0, respectively. The fundamental frequency f_0 here corresponds to the frequency of the secondary instability and $\beta \approx 523.6\ m^{-1}$ to the spanwise wavenumber of the stationary crossflow mode (0,1). At $x_c/c \approx 0.75$ rapid growth of the secondary eigenmode represented by the packet of Fourier modes (1,n) sets in which further downstream triggers an even more rapid growth of a packet of nonlinearly generated modes (2,n) at twice the fundamental frequency.

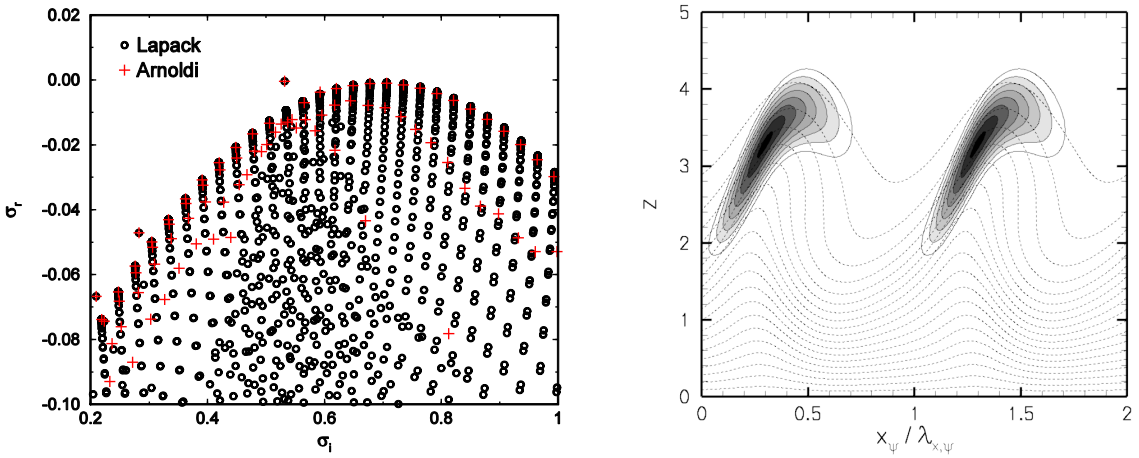

Figure 78: Left: Temporal secondary eigenspectrum at x_c/c=0.70 showing an isolated marginally stable secondary eigenmode which has a dimensional frequency of 2640 Hz. σ_i here denotes the nondimensional frequency and σ_r its nondimensional temporal growth rate. Compared are the results from two different numerical approaches (LAPACK routine and in-house routine of Arnoldi-type) eigenvalue computations. Right: Corresponding rms-isocontours of the v_v-velocity component of the marginally stable secondary eigenmode in a wall-normal plane where y_v denotes the direction of the primary vortex axis.

The corresponding disturbance structures in physical space are visualized in Figure 79 for chord position $x_c/c\approx0.85$. For f≈2640 Hz a single maximum in rms-amplitude per fundamental spanwise wave length λ_c develops (Figure 79 left). The region of highest rms-amplitude is very much localized in space and spatially coincides with a region of high shear in the time-averaged flow field which is typical for a high-frequency secondary instability. Qualitatively the same structure can be found also further upstream up to the position where the secondary mode was initialized, confirming the correct initialization of the secondary mode and its representation by the packet of Fourier modes (1,n) within the PSE approach. For f≈5280 Hz two maxima per fundamental spanwise wave length λ_c are noted instead (Figure 79 right). Further downstream more complex mode interaction scenarios develop due to the further increased disturbance amplitudes resulting in more complicated spatial structures in the rms-distributions (not shown here). Moreover, the stationary modes no longer remain unaffected by the presence of the unsteady modes as can be seen from a comparison with corresponding results from a computation without initialization of the secondary disturbance (Figure 77 left). At this stage these nonlinear interactions also lead to an additional steep rise in skin friction before the calculation stops converging at $x_c/c\approx0.93$, whereas in the case without secondary instability mode included the increase in skin-friction coefficient levels off in the saturation region of the stationary crossflow vortices (Figure 77 right).

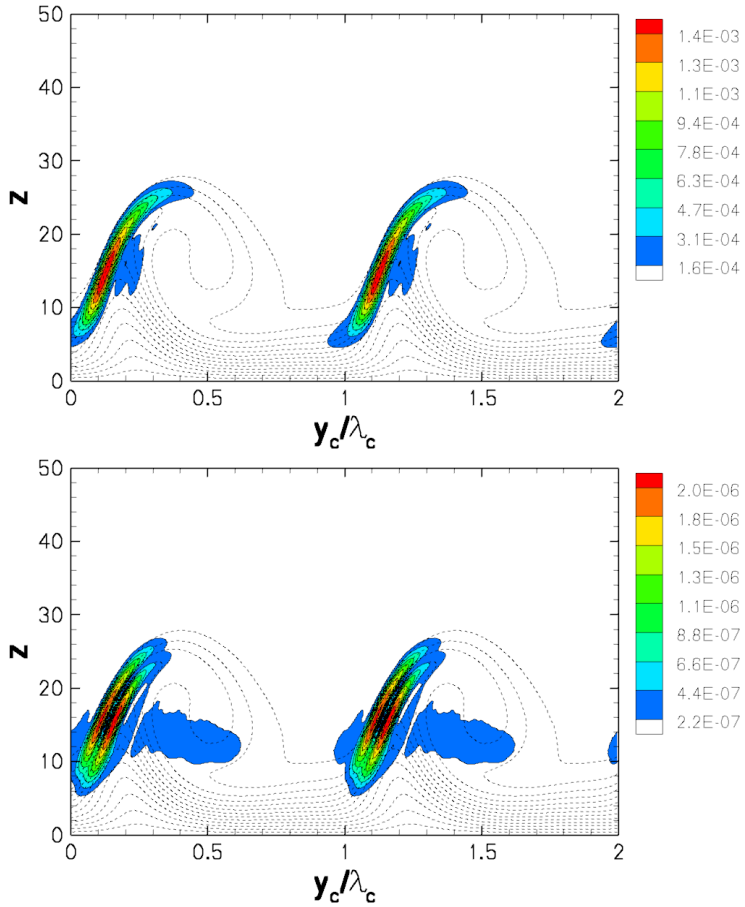

Figure 79: rms-isocontours of the v_v-velocity component in a wall-normal plane at chord position $x_c/c=0.85$ plotted on top of the isolines (dashed) of the time-averaged velocity component in y_v-direction. The y_v-direction is locally aligned with the direction of the primary stationary crossflow vortex axis. Upper: Secondary instability mode with a frequency f≈2640 Hz represented in the PSE computations by Fourier modes (1,n) with -16 ≤ n ≤ +16. Lower: The corresponding first higher harmonic with a frequency f≈5280 Hz represented by the modes (2,n).

8 Stability analysis of fully three-dimensional

8.1 Selected geometry and flow cases

CIRA performed a bibliographic research in order to find select suitable reference geometries for the application of transition prediction methods. The result of this bibliography search has evidenced that in Europe exist only few public geometries available for numerical. Finally it was decided to use the following geometries:

- Laminar wing developed by CIRA and Piaggio Aero Industries S.p.A. in the framework of an Italian national program called VITAS:
  - Experiments performed at HST German-Dutch Wind Tunnels
  - Natural laminar flow visualization have been performed using two Thermovision A40 M Infrared cameras
  - Unsteady flow measurements with kulites pressure transducers
  - Mach Range Investigated 0.4 – 0.6 – 0.7 – 0.75 – 0.8
  - Reynolds number Range Investigated 4 10^6 – 8 10^6 – 10 10^6

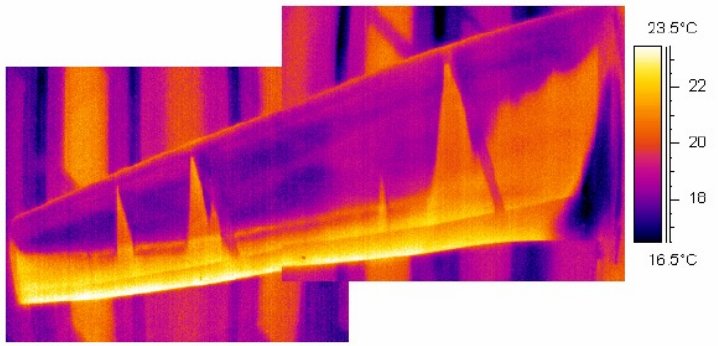

Figure 80: Example of IR images for VITAS geometry. M=0.78, Re=8mil, CL=0.4.

- JAXA NEXST-1 (**N**ational **EX**periment **S**upersonic **T**ransport) program with the objective of validating the NLF concept on a supersonic demonstrator:
  - Total length = 11,5 m, Total width = 4,72 m
  - Transition detection by hot films and Preston tube
  - Flight conditions: H = 18 km, M_0 = 2, Re_c = 14x10^6 (with C = 2,754 m)

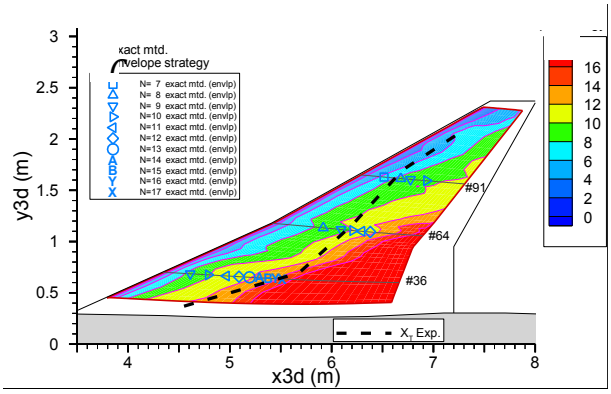

Figure 81: N-factors for JAXA flight test comaputed based on infinite swept wing approximation. $N_T \approx 15$ on the inner wing, $N_T \approx 7$ on the outer wing.

8.2 Flow computations

8.2.1 VITAS geometry

In order to obtain the meanflow for further stability analysis, Piaggio has generated a computational mesh and performed Euler and RANS analyses for the defined test case (VITAS laminar wing) for the four test case conditions.

	M	*CL*	*Re*
Condition 1 (C1)	0.75	0.5	8.0 mln
Condition 2 (C2)	0.78	0.45	8.0 mln
Condition 3 (C3)	0.75	0.45	8.0 mln
Condition 4 (C4)	0.75	0.5	4.0 mln

Table 4: Test case conditions analyzed.

The first condition (C1) represents the low speed cruise condition, while the second (C2) corresponds to the fast cruise condition. The third condition was chosen to consider the effects of the Mach number (with respect to the C2 condition) and of the lift coefficient (with respect to the C1 condition). The last condition defined was aimed to study Reynolds effects with respect to the C1 condition.

It has been noticed that all the results obtained show the same trend: there is not a good matching between numerical and experimental results. In particular, Euler results show a second expansion peak in the rear part of the upper side of the airfoil. This second expansion is not present when RANS evaluations are carried out, due to the viscous effects neglected by Euler model. In cooperation with CIRA further Euler evaluations have been performed on the inner section with MSES code. The results obtained confirm the trend observed using PAI's commercial flow solver (CFD++).

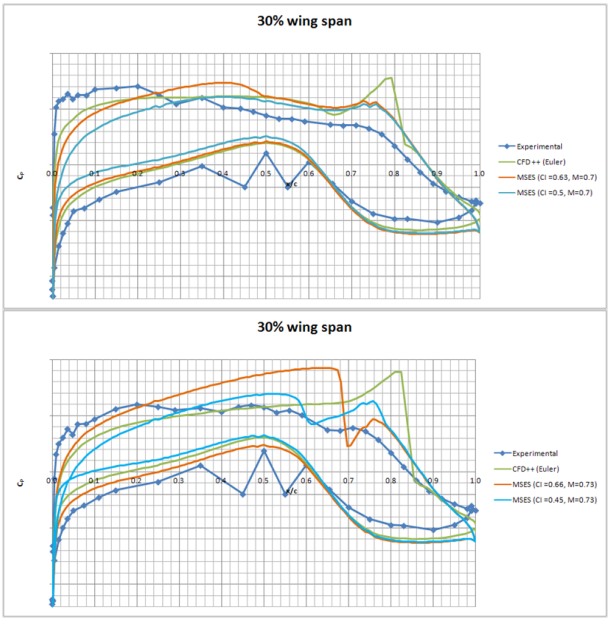

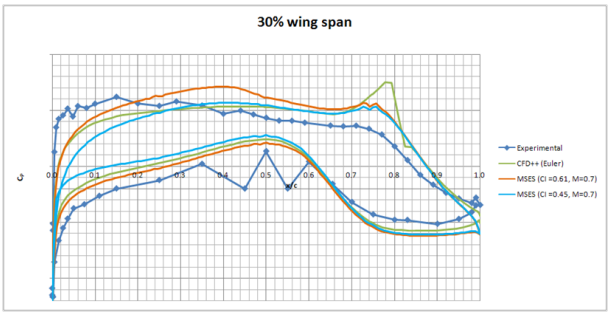

Figure 82: Comparison between the experimental and Euler chord-wise pressure coefficient distribution at 30% of the half span for several test case conditions.

It must be noticed that in the fast cruise condition (second picture above reported) a big mismatching between the numerical results is found, pronounced by different positions of the second expansion. Furthermore, a shock wave is visible, even if the experiment does not provide evidence of it. In particular, the CFD++ solution shows the rearmost shock wave location, while the foremost is obtained with MSES at CL = 0.45. Furthermore, MSES predicts a second expansion downstream the shock wave, while CFD++ shows it in correspondence of the shock wave location.

Further, simulations were performed with higher resolution in spanwise direction to meet the requirements for stability analysis to be performed usin ray-tracing theory and 3D PSE.

Based on the Euler solutions delivered by PIAGGIO for the four selected cases, CIRA has performed 3D boundary-layer simulations using 3C3D code. The solutions of boundary-simulations has been extracted at different spanwise sections and stored in EURORANS format. The data has been delivered to other partners for further 3D stability analysis.

A first qualitative comparison between experimental data and contour map of N-factor showed a good agreement. Transition abscissa location will be provided in a different file.

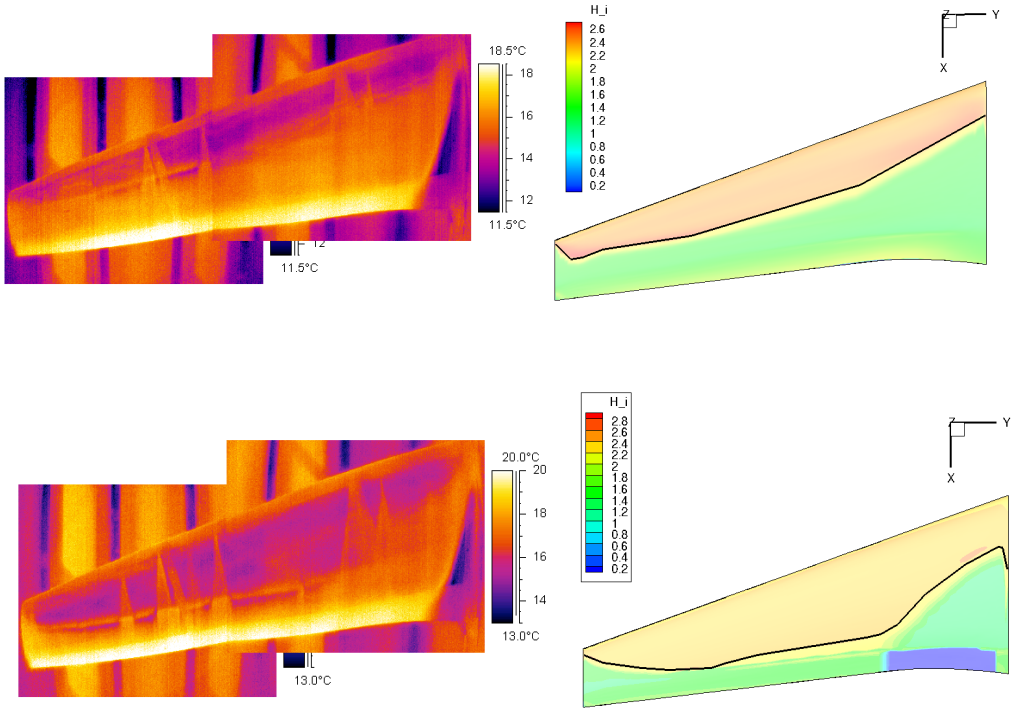

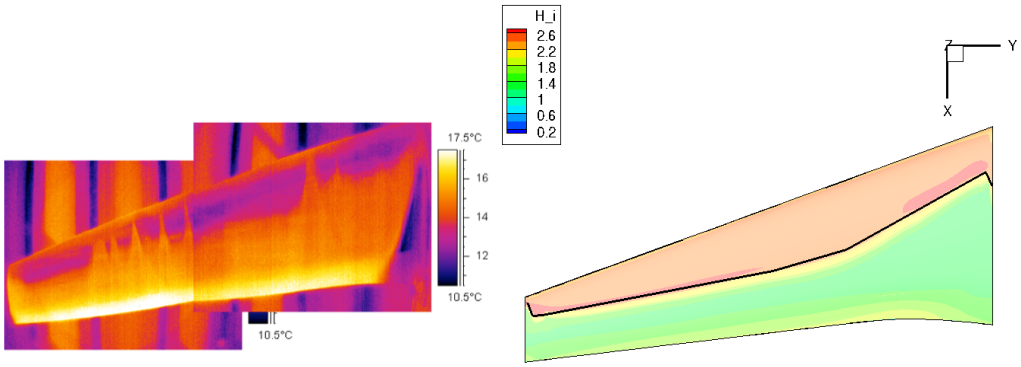

Figure 83: IR visualization (left) and N factor contour map (right) for cases TC1 (upper), TC2 (middle) and TC3 (lower).

The data is supposed to be used for the 3D stability analysis (through ray-theory and 3D PSE). First simulations showed that the spanwise distribution of the generated flow was not enough for stability analysis. Therefore, a new set of RANS computations by PIAGGIO and BL computations by CIRA was performed.

8.2.2 JAXA geometry

ONERA delivered the boundary-layer edge velocity distribution for JAXA experiments to those partners who signed the Letter of Agreement. Further, 3D boundary-layer computations were performed and meanflow profiles (in EUROTRANS format) at different cross sections have been delivered to partners involved.

The preliminary computations for JAXA case showed that the spanwise resolutions of the available boundary-layer profiles are not enough for the stability computations. Therefore, a Matlab code was developed by FOI to perform the interpolation in spanwise directions as well as in the wall normal direction (some of partners 3D stability code requires constant number of points at all stations). The code was distributed among partners involved in WP4.

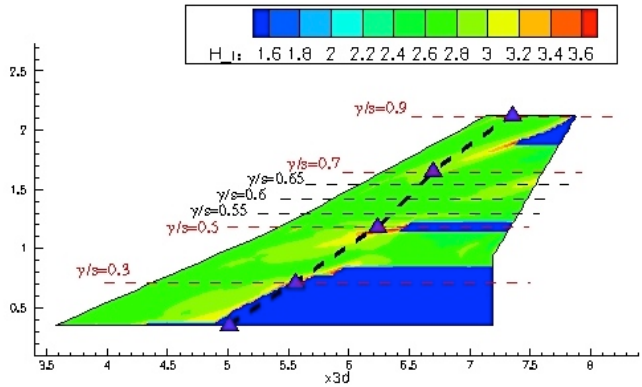

Figure 84: Shape-factor distribution on wing of JAXA demonstrator. 3D boundary-layer computations performed by ONERA. Thin dashed lines correspond to cross sections along which velocity profiles have been extracted

8.3 Stability analysis

8.3.1 VITAS geometry

UNISA and CIRA, have developed a code for the stability analysis of 3D boundary layers based on the theory of ray tracing. The application of such theory to the stability analysis of laminar flows

permits us to take into account the boundary-layer growth and the dependency of the wave speed on the propagation direction. The instability waves are assumed to be proportional to exp[iθ(x, y, z, t)], with the frequency and wavelengths defined locally as derivatives of the phase function θ. The dispersion relation takes the form of a first-order partial differential equation for θ. The solution of this equation by the method of characteristics leads to the ray equations. The code has been developed in order to compute the stability of boundary layers over 3D swept wings. The disturbance equations are derived by means of the multiple-scale technique and using an asymptotic expansion for the disturbances in terms of the small parameter Re^{-1}. The *O(0)* approximation is governed by a set of equations formally identical to that resulting from the parallel flow assumption. The *O(1)* approximation gives the correction to the wave amplification due to the boundary-layer growth.

The code has been validated using a test case available from EUROLIFT II. The calculations provide the rays along which the disturbance propagates. By computing the N factors along these rays for different frequencies, it is possible to build a spatial map representing the most amplified iso-N factor curves (see Figure 85).

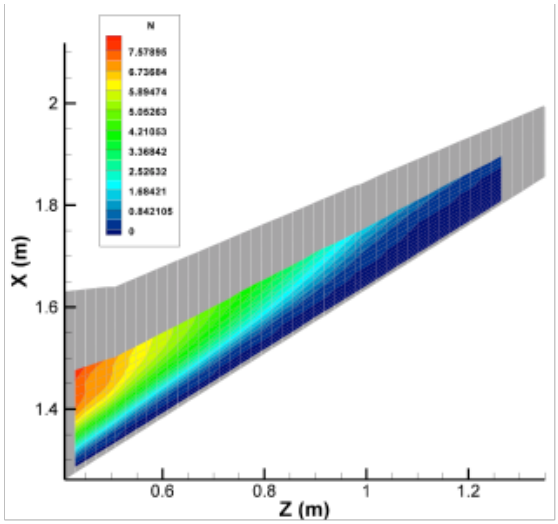

Figure 85: N-factor map calculated using ray-tracing theory.

The analyses of VITAS test cases included both classical 2.5D and ray-tracing approach. The classical analysis covered 4 different test cases including effects of Mach number and angle of attack. The 3D stability analyses using ray-tracing theory were performed for VITAS wing corresponding to the TC2 case. This test case was chosen because 2.5D linear stability analyses showed that the highest N-factor values were achieved on all the considered nine sections.

In Figure 86 the N-factor contour on the upper side of the TC2 for VITAS wing is shown. These N-factors, computed by ray-tracing theory, correspond to the highest possible amplifications and is obtained by considering perturbations initiated along the span of the wing. Figure 87 shows the area of the wing surface where the most amplified perturbations are generated. The colour indicates the maximum N-factor reached by these perturbations. The identification of the location of this area is of paramount importance because it provides information concerning the region that strongly affects the transition. The knowledge of this type of maps allows locating the regions of the wing which are particularly critical for the transition of the boundary layer from laminar to turbulent, due to their high sensitivity to disturbances. This information is extremely important for the design and construction of a laminar wing since these critical regions require particular care if laminar flow is desired.

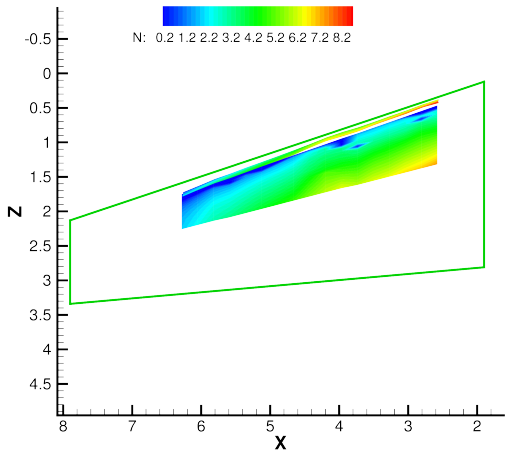

Figure 86: N factor contour - TC2 VITAS wing.

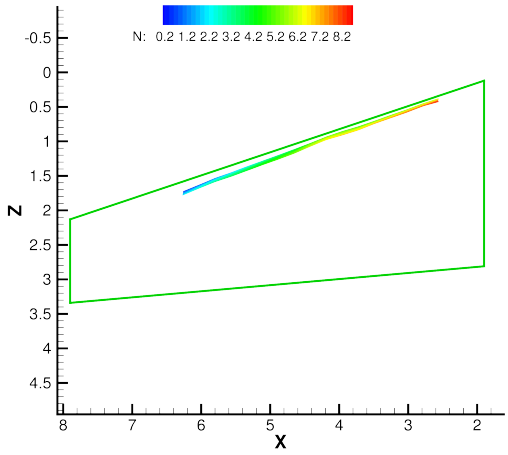

Figure 87: Region of origin of the disturbance - TC2 VITAS wing.

8.3.2 JAXA geometry

The local and nonlocal stability analysis performed by FOI, DLR and CIRA gave unexpected low N-factors. Despite use of different integrations path for N-factor computations, this mater was not solved. Thus partners involved in these activities decided to concentrate their efforts on other activities of the project.